JCI The Journal of Clinical Investigation

Efferocytosis activates a DNMT3A-mediated oxidized DNA repair pathway to enable tissue resolution

Kleopatra Avrampou, Santosh R. Sukka, David Ngai, Patrick Ampomah, Xiaobo Wang, George Kuriakose, Jacob Glass, Bernhard Dorweiler, Hanna Winter, Lars Maegdefessel, Hanrui Zhang, Aaron Viny, Ira Tabas

J Clin Invest. 2026. https://doi.org/10.1172/JCI203265.

Research In-Press Preview **Cell biology** **Vascular biology**

Graphical abstract

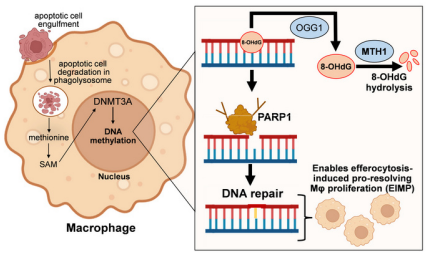

Efferocytosis activates a DNMT3A-mediated oxidized DNA repair pathway to enable tissue resolution

Kleopatra Avrampou[1], Santosh R. Sukka[1], David Ngai[1], Patrick Ampomah[1], Xiaobo Wang[1], George Kuriakose[1], Jacob Glass[2], Bernhard Dorweiler[3], Hanna Winter[4], Lars Maegdefessel[5], Hanrui Zhang[1], Aaron Viny[1], Ira Tabas[1,6,7]

[1]Department of Medicine, Columbia University Irving Medical Center, New York, New York, USA. [2]Center for Epigenetics Research, Memorial Sloan Kettering Cancer Center, New York, NY, USA. [3]Department of Vascular and Endovascular Surgery, University of Cologne, Faculty of Medicine and University Hospital Cologne, Cologne, Germany. [4]Institute of Molecular Vascular Medicine, TUM Klinikum, Technical University of Munich, Munich, Germany. [4]Department of Physiology and Cellular Biophysics and [5]Department of Pathology and Cell Biology, Columbia University Irving Medical Center, New York, New York, USA.

Address correspondence to: Kleopatra Avrampou or Ira Tabas, Department of Medicine, Columbia University Irving Medical Center, 630 W. 168th Street, New York, New York 10032, USA. Email: ka2897@columbia.edu or iat1@columbia.edu.

Abstract

Efferocytosis, the clearance of apoptotic cells by macrophages, promotes tissue resolution. Efficient resolution requires efferocytosis-induced macrophage proliferation (EIMP) to expand pro-resolving macrophages. Here, we show that efferocytosis activates base excision repair (BER) to remove 8-OHdG from DNA, enabling EIMP. Mechanistically, efferocytosis promotes poly(ADP-ribose) polymerase-1 (PARP1) chromatin binding and PARylation to facilitate DNA repair complex assembly, and increases nuclear MTH1/NUDT1, which hydrolyzes 8-OHdG. Both processes require DNA-methyltransferase-3A (DNMT3A), which is activated during efferocytosis. Using a model where dexamethasone-induced thymocyte apoptosis triggers efferocytosis-mediated thymic repair, we showed that DNMT3A is required for increases in nuclear PARP1/MTH1, oxidized DNA suppression, EIMP in thymic macrophages, and thymic repair. We next studied a human-relevant model of atherosclerosis regression, where efferocytosis drives protective lesional fibrous cap thickening. We compared WT mice with a model of DNMT3A-clonal hematopoiesis (CH), in which loss-of-function DNMT3A mutations promote atherosclerotic disease. Atherosclerosis regression in WT mice led to decreased nuclear 8-OHdG and increases in nuclear PARP1/MTH1 and EIMP in lesional macrophages and fibrous cap thickening, all of which were impaired in DNMT3A-CH regression. These findings reveal that efferocytosis initiates a BER pathway to allow macrophage proliferation for tissue resolution, with possible therapeutic relevance to atherosclerosis regression and DNMT3A-CH.

Introduction

Efferocytosis, the process through which macrophages engulf and clear apoptotic cells (ACs), prevents secondary necrosis and promotes tissue resolution (1-3). Pathological impairment of efferocytosis-induced resolution drives many disease processes, including autoimmune, pulmonary, neurodegenerative, and atherosclerotic diseases (1-3). Efferocytosis triggers several pathways that reprogram macrophages to synthesize tissue repair factors, such as interleukin-10 (IL-10) and transforming growth factor-β1 (TGF-β1), and to acquire specialized features that enable the sequential uptake of multiple ACs, called continuing efferocytosis, which is critical for tissue repair in vivo (4-12). Several mechanisms linking efferocytosis to pro-resolving macrophage reprogramming have been identified, including efferocytosis receptor-mediated signaling pathways, alterations in macrophage energy metabolism, and pathways triggered by molecules derived from the phagolysosomal degradation of ACs (6-9, 12-15). For example, AC-derived methionine, after conversion to S-adenosylmethionine, activates DNMT3A-mediated DNA methylation, which enhances a pro-resolving ERK1/2-TGFβ1 pathway in efferocytosing macrophages (8). As another example, AC-derived nucleotides trigger a Myc-mediated proliferation pathway, known as efferocytosis-induced macrophage proliferation (EIMP) (7, 15). EIMP expands the pool of pro-resolving macrophages to enhance continuous AC clearance and tissue repair in vivo (7, 15), and recent work has suggested a broad impact of EIMP in a variety of in vivo settings (16-22). In this context, identifying additional mechanisms linking efferocytosis to pro-resolving macrophage reprogramming and understanding how macrophages integrate distinct efferocytosis-induced reprogramming pathways to carry out effective resolution represent key goals in this critical area of biomedical research.

During studies aimed at identifying additional pro-resolving effects of the methionine-DNMT3A pathway, we made the unexpected observation that efferocytosis lowers nuclear 8-hydroxy-2'-deoxyguanosine (8-OHdG), a marker of oxidized DNA, and that this process requires DNMT3A. Mechanistically, efferocytosis-induced DNA methylation by DNMT3A enhances chromatin binding of poly(ADP-ribose) polymerase 1 (PARP1), facilitating base excision repair (BER) complex formation, while concurrently increasing nuclear MutT homolog 1 (MTH1; gene NUDT1) to hydrolyze excised 8-OHdG. We demonstrate that this DNMT3A-mediated oxDNA-suppression pathway occurs in efferocytosing macrophages in vivo and is required for EIMP, likely by enabling DNA synthesis, and facilitates tissue resolution. In particular, the pathway plays a key role in a human-relevant model of atherosclerosis regression induced by cholesterol lowering (23-27), where efferocytosis-driven resolution, including EIMP, promotes the formation of a protective fibrous cap over atherosclerotic plaques (6, 7, 9, 28). We now show the role of the DNMT3A-BER pathway in regression-induced cap thickening. For this purpose, we used a model of DNMT3A clonal hematopoiesis (CH), reflecting human clinical data showing that somatic DNMT3A loss-of-function mutations are associated with increased risk of atherosclerotic disease (29-40). We also found that lesional macrophages in unstable regions of human

carotid atheroma displayed elevated levels of 8-OHdG and reduced nuclear PARP1 and MTH1 compared to stable regions.

Thus, we have identified what we believe to be a previously unrecognized mechanism linking efferocytosis to pro-resolving macrophage reprogramming involving a BER-induced oxDNA suppression pathway activated by DNMT3A-mediated DNA methylation. This pathway contributes to tissue resolution, including in the critical process of atherosclerosis regression, with possible relevance to DNMT3A-CH. The role of the pathway in EIMP suggests integration between two AC-cargo-driven resolution pathways: one involving AC-derived methionine and DNMT3A and the other involving AC-derived nucleotides, together supporting the expansion of pro-resolving macrophages.

Results

Efferocytosis induces the suppression of nuclear oxidized DNA in a DNMT3A-dependent manner. While studying responses of macrophages to the uptake of Jurkat cells rendered apoptotic by UV irradiation (apoptotic cells, ACs), we observed a previously unknown phenomenon in which efferocytosis suppresses basal levels of nuclear oxDNA. Specifically, we incubated mouse bone marrow-derived macrophages (BMDMs) in the absence or presence of ACs for 45 minutes, which stimulates efferocytosis, followed by AC removal and a 1-hour chase period. The macrophages were then immunostained for the oxDNA marker, 8-OHdG, and various nuclear markers. The data show that 8-OHdG mean fluorescence intensity (MFI) in nuclei, identified by immunostaining for histone 2A (H2A) or lamin B1, was suppressed by efferocytosis in macrophages (**Figure 1, A and B, top rows of images**). To understand how efferocytosis causes the suppression of nuclear oxDNA, we explored pathways known to be activated by AC uptake in macrophages. One such pathway involves AC-derived methionine, which increases the methyl donor S-adenosylmethionine (SAM) and SAM-dependent DNMT3A-mediated DNA methylation (8). We found that efferocytosis-induced suppression of nuclear oxDNA was not seen in BMDMs lacking DNMT3A (DNMT3A-KO) (**Figure 1, A and B, bottom row of images**), which could not be explained by impaired primary efferocytosis in DNMT3A-KO versus control macrophages (**Supplemental Figure 1A**). Efferocytosis also decreased total cellular 8-OHdG in a DNMT3A-dependent manner after a 1-hour chase, and this suppression was also observed after a 3-h chase but not after a 6-hour or 24-hour chase (**Supplementary Figure 1B**).

Moving beyond mouse BMDMs, we observed similar findings when comparing efferocytosing human monocyte-derived macrophages treated with siDNMT3A versus scrambled RNA (**Figure 1C and Supplementary Figure 1C**). Moreover, we also tested human apoptotic macrophages generated by staurosporine treatment, which reflects the major source of apoptotic cells in atherosclerosis (41) (see final section). The results were like those observed using apoptotic Jurkat cells: efferocytosis suppressed nuclear 8-OHdG in wild-type (control) but not DNMT3A-KO macrophages (**Figure 1D**).

Our previous work showed that DNMT3A-mediated DNA methylation in efferocytosing macrophages was

driven by a methionine—S-adenosyl methionine (SAM) pathway that utilized the methionine from the engulfed and degraded ACs (8). To test the relevance of this AC-cargo pathway here, we pretreated macrophages with bafilomycin A1, a lysosomal vacuolar ATPase inhibitor that blocks the phagolysosomal degradation of ACs during efferocytosis (42-45). Inhibition of lysosomal degradation blocked the efferocytosis-induced suppression of nuclear oxDNA (**Supplementary Figure 1D**), indicating that apoptotic cell degradation is required for this effect. Moreover, inhibition of SAM synthesis using the methionine adenosyltransferase 2A (MAT2A) inhibitor PF-9366 similarly blocked efferocytosis-induced suppression of nuclear oxDNA (**Supplementary Figure 1E**). Finally, as DNMT3A can affect cells by both DNA methylation-dependent and -independent mechanisms (42-45), we tested whether DNA methylation is required for efferocytosis-induced suppression of nuclear oxDNA. For this purpose, we used macrophages treated with the DNA-methylation inhibitor 5-AzaC or transduced with the DNA demethylase Tet1. Both interventions blocked efferocytosis-induced suppression of oxDNA in WT macrophages (**Figure 1, E and F**). These combined data reveal a pathway triggered by efferocytosis in which DNMT3A-mediated DNA methylation suppresses the basal level of 8-OHdG in macrophages. In the following sections, we explore the mechanism of 8-OHdG suppression and, most importantly, its functional significance.

Efferocytosis-induced suppression of oxDNA is dependent on PARP1 and MTH1. We hypothesized that suppression of 8-OHdG by efferocytosis could result either from reduced reactive oxygen species (ROS) production or activation of DNA repair. Using an ROS-sensitive fluorogenic probe (CellROX™), we found that ROS increased with efferocytosis, which is consistent with a previous study from our group (27), but DNMT3A deletion did not suppress efferocytosis-induced ROS (**Supplemental Figure 2A**). We therefore investigated whether efferocytosis, through DNMT3A, promoted DNA repair. To begin, we showed that the double-strand break marker γH2AX was similar between DNMT3A-KO and control macrophages before and after efferocytosis (**Supplementary Figure 2B)**, suggesting that repair of double-strand DNA breaks was not involved. We then explored a possible role for base excision repair (BER) of oxDNA in efferocytosing macrophages. BER repair of oxDNA involves excision of 8-OHdG by 8-oxoguanine glycosylase (OGG1) followed by (i) repair of the excised DNA by a protein complex in which PARP1-mediated PARylation plays a key role by promoting the recruitment of the DNA-repair proteins; and (ii) hydrolysis of the excised 8-OHdG by MTH1 to prevent 8-OHdG reincorporation into DNA during DNA replication (46, 47) (**Supplemental Figure 2C**).

In support of a role for BER, we showed that silencing OGG1 blocked efferocytosis-induced suppression of nuclear oxDNA (**Figure 2A and Supplementary Figure 2D**). Focusing next on PARP1, we found that its nuclear localization increased with efferocytosis in WT but not DNMT3A-KO macrophages (**Figure 2B**). Efferocytosis did not significantly alter total cellular *Parp1* mRNA or protein levels (**Supplemental Figure 2E and F**). Most importantly, silencing PARP1 in WT macrophages blocked efferocytosis-induced suppression of oxDNA (**Figure 2C and Supplemental Figure 2G**). Similar results were observed using the PARP inhibitor

N-(6-oxo-5,6-dihydro-phenanthridin-2-yl)-N,N-dimethylacetamides HCl (PJ34) (48), which inhibits PARP1 enzymatic activity and PAR chain formation, both in mouse bone marrow-derived macrophages and human monocyte-derived macrophages (**Figure 2, D and E**).

A key step in PARP1-mediated DNA repair is binding of PARP1 to chromatin and protein PARylation, which induces PARP1 enzymatic activation and PARylation of PARP1 and associated proteins (49). Accordingly, we found that both PARP1 chromatin binding and PARylation activity were increased by efferocytosis in WT macrophages, but much less so in DNMT3A-KO macrophages (**Figure 2F**). To link to DNA methylation, we first showed that efferocytosis-induced nuclear PARP1 was accompanied by an increase in 5-methylcytosine, associated with an increase in nuclear PARP1 (**Supplemental Figure 2H**). Further, 5-AzaC treatment of macrophages blocked efferocytosis-induced PARP1 chromatin association as assessed by immunoblot (**Figure 2F**), and transduction of macrophages with Tet1 demethylase blocked efferocytosis-induced nuclear PARP1 as assessed by immunofluorescence microscopy (**Figure 2G**). Thus, efferocytosis-induced nuclear PARP1, like suppression of 8-OHdG, is mediated by the DNA methyltransferase activity of DNMT3A.

We next turned our attention to MTH1. As with PARP1, efferocytosis increased nuclear MTH1 in WT but not in DNMT3A-KO macrophages, as measured by immunofluorescence microscopy or immunoblot of the nuclear soluble fraction in mouse and human macrophages (**Figure 3, A-C**). Efferocytosis did not significantly alter total cellular *Nudt1* mRNA or MTH1 protein levels (**Supplemental Figure 3A and B).** Moreover, silencing MTH1 (siNudt1) or treatment with the MTH1 inhibitor TH287 (50) prevented the suppression of 8-OHdG in WT macrophages (**Figure 3, D and E, and Supplemental Figure 3C**). These effects, and those above related to siParp1 and PJ34, could not be explained by inhibition of primary AC uptake (**Supplemental Figure 3, D and E**). As with PARP1, efferocytosis-induced nuclear MTH1 in WT macrophages was inhibited by 5-AzaC and Tet1 transduction, supporting a role for DNA methylation (**Figure 3, F and G**). Most importantly, retroviral transduction of DNMT3A-KO macrophages with MTH1 corrected the defect in efferocytosis-induced suppression of oxDNA in these cells (**Figure 3H and Supplemental Figure 3F**). Collectively, these data support a pathway in which efferocytosis promotes the lowering of oxDNA through a DNMT3A-dependent PARP1/MTH1-mediated DNA repair pathway.

The suppression of oxDNA is required for efferocytosis-induced macrophage proliferation. Efferocytosis-induced changes in macrophages are often linked to the activation of tissue resolution pathways, and thus we wondered if efferocytosis-induced suppression of oxDNA was required for a specific resolution process. We considered a key tissue resolution process called efferocytosis-induced macrophage proliferation (EIMP), because EIMP requires DNA synthesis (7). EIMP, which is triggered by AC-derived nucleotides and Myc upregulation, expands the pool of pro-resolving efferocytic macrophages during tissue injury and is essential for the proper clearance of apoptotic cells and tissue repair in vivo (7, 15-22). Given

that impaired repair of oxDNA can block cell proliferation in other settings (51), we hypothesized that efferocytosis-induced suppression of oxDNA might be necessary for EIMP when macrophages are exposed to ACs during tissue injury.

To explore this hypothesis in vitro, we incubated WT and DNMT3A-KO macrophages with ACs to induce efferocytosis. As previously reported (7), the number of WT macrophages increased when the macrophages were observed 24 hours later, but this was not observed with the DNMT3A-KO macrophages (**Figure 4A**). As additional markers of EIMP, we showed previously that efferocytosis in macrophages increased both the expression of the proliferation marker Ki67 and the incorporation of 5-ethynyl-2'-deoxyuridine (EdU) into DNA (7). Both endpoints were lower in DNMT3A-KO versus WT macrophages after AC exposure (**Figure 4B**), whereas Ki67 and EdU levels did not differ between genotypes in the absence of ACs (**Supplementary Figure 4, A and B**). A marker of oxDNA-induced cell-cycle arrest is the elevation of the cell-cycle checkpoint response protein, $p21^{WAF1/Cip1}$ (CDKN1A), which is an inhibitor of cyclin-dependent kinase (CDK) that arrests cells in G_1/G_2 phase (52). We found that p21 expression following efferocytosis was higher in DNMT3A-KO versus WT macrophages, with no difference between macrophages incubated in the absence of ACs (**Figure 4C, Supplementary Figure 4C**), suggesting that failure of efferocytosis-induced suppression of oxDNA causes cell cycle arrest. We also considered a role for p53 levels, as p21 is a known target of p53, but the expression of p53 was not altered by efferocytosis, and pharmacological inhibition of p53 with pifithrin-α (PFTα) (53) did not affect p21 expression (**Supplementary Figure 4, D and E**). These data suggest that p21 is increased by a p53-independent mechanism (54) in efferocytosing DNMT3A-KO macrophages, and, given the role of p53 in double-strand DNA breaks (55), they are consistent with the negative γH2AX data above.

We next tested the role of PARP1 and MTH1 in EIMP, i.e., as a link to the aforementioned DNMT3A-dependent oxDNA repair mechanism. We found that inhibition of PARP1 with PJ34 or MTH1 with TH287 blocked EIMP in WT mouse macrophages, as measured by cell number or Ki67 expression (**Figure 4, D and E**). PJ34 also lowered Ki67 expression in WT human macrophages (**Figure 4F**). Conversely, retroviral transduction of efferocytosing DNMT3A-KO macrophages with MTH1 increased Ki67 expression and the percentage of macrophages incorporating EdU into their DNA (**Figure 4G**). Thus, the DNMT3A/PARP1/MTH1-mediated oxDNA repair mechanism in efferocytosing macrophages is necessary for EIMP in vitro.

Evidence of DNMT3A-mediated suppression of oxDNA in efferocytosing macrophages in vivo. To determine if DNMT3A-mediated suppression of oxDNA occurs when macrophages are exposed to ACs in vivo, we turned to a well-established model of efferocytosis-induced tissue resolution in which mice are injected with dexamethasone (DEX) (56). Within 4 hours after DEX injection, apoptotic thymocytes increase, which initiate efferocytosis by thymic macrophages (6, 56). This phase of efferocytosis reflects in vivo the process referred to primary efferocytosis in vitro. Efferocytosis-induced repair processes then follow, and by

18 hours, tissue repair is well underway (6-9). However, mice with defective efferocytosis or impaired efferocytosis-induced resolution signaling show elevated thymic necrosis at the 18-hour time point (6-9). Efferocytosis observed at 18 hours is representative of continuing efferocytosis, which is the sequential clearance of multiple ACs by a single macrophage, and it is a critical process for tissue repair (4-9).

To begin, we transplanted irradiated wild-type (WT) mice with bone marrow from control *Vav1cre*$^{+/-}$ (control) or *Dnmt3a*$^{fl/fl}$*Vav1cre*$^{+/-}$ to create hematopoietic-DNMT3A-KO (H-DNMT3A-KO) mice. After 4 weeks of recovery, the mice were injected with PBS or DEX. Focusing first on the dexamethasone-treated mice, we documented that DNMT3A expression in thymic macrophages was significantly diminished in the KO cohort (**Figure 5A, Supplementary Figure 5A**). Moreover, we verified the presence of efferocytosing macrophages in the thymus, measured as the ratio of macrophage-associated to free TUNEL$^+$ cells (**Figure 5B**). As mentioned above, efferocytosis at 4 hours reflects mostly primary efferocytosis. Thus, the finding that the values for control and DNMT3A-KO are similar in Figure 5B is consistent with our in vitro data showing intact primary efferocytosis in DNMT3A-KO macrophages (refer to Supplemental Figure 1A). We then analyzed all four groups (PBS or DEX in control and H-DNMT3A-KO mice) for nuclear 8-OHdG in thymic macrophages. Macrophage nuclear 8-OHdG was lower in the thymi of DEX- versus PBS-injected control mice, which correlates with increased efferocytosis by thymic macrophages in the DEX cohort, but nuclear 8-OHdG in thymic macrophages was not lower in DEX- versus PBS-injected H-DNMT3A-KO mice (**Figure 5C**). Moreover, nuclear PARP1 and MTH1 were increased in the thymic macrophages of DEX- versus PBS-injected control mice but not in DEX- versus PBS-injected KO mice (**Figure 5, D and E**). Importantly, when DEX-treated WT mice were injected with PJ34 to inhibit PARP1 or with TH287 to inhibit MTH1, nuclear 8-OHdG was elevated in thymic macrophages compared to mice injected with vehicle control (DMSO) (**Figure 5F**). As with our in-vitro data, this finding was not due to inhibition of primary efferocytosis by these inhibitors (**Supplemental Figure 5B**). These data provide strong evidence that the DNMT3A/PARP1/MTH1 pathway of efferocytosis-induced oxDNA suppression occurs in vivo.

A major goal in this experiment was to determine if EIMP in thymic macrophages, which is stimulated by DEX treatment in WT mice at 18 hours due to the increase in apoptotic thymocytes (7, 15), was blunted in DEX-treated H-DNMT3A-KO mice. We have shown previously that H-DNMT3A-KO in DEX-treated mice compromises continuing efferocytosis in thymic macrophages, assayed by quantifying the ratio of macrophage-associated versus free TUNEL$^+$ cells (8). H-DNMT3A-KO also causes thymic necrosis, identified by regions of hypocellularity and/or small, fragmented nuclei (8). Here, we verified both of these findings in this experiment (**Supplemental Figure 5, C and D**). We now show that EIMP, which we assay by quantifying the percentage of thymic macrophages expressing Ki67 (7, 15), was markedly lower in the thymi of DEX-treated H-DNMT3A-KO versus control mice (**Figure 5G**). Moreover, treatment with the MTH1 inhibitor TH287 blocked continuing efferocytosis and EIMP in the thymi of DEX-treated WT mice (**Figure 5, H and I**), accompanied by increased thymic necrosis (**Figure 5J**). Note the total number of thymic macrophages was

not affected by either DNMT3A-KO or TH287 despite lower EIMP (**Supplemental Figure 5, E and F**), which is consistent with the concept that EIMP increases the relative proportion of pro-resolving macrophages in tissues rather than the total number of macrophages (7). In sum, these data link the DNMT3A/PARP1/MTH1 oxDNA repair pathway during efferocytosis to EIMP and tissue resolution in vivo.

Evidence of impaired efferocytosis-induced suppression of oxDNA in atherosclerosis regression in a model of DNMT3A clonal hematopoiesis. DNMT3A LoF variants are a common cause of clonal hematopoiesis (CH), which is a risk factor for atherosclerotic cardiovascular disease (CVD) (29-38). We therefore investigated whether a CVD-relevant DNMT3A-CH mutation, R882H (R878H in mice) (35, 57), impairs efferocytosis-induced suppression of oxDNA and EIMP in an atherosclerosis setting in mice. We used an R878H/WT chimeric bone marrow-transplantation protocol to reflect the chimeric nature of hematopoietic CH mutations in humans. As a human-relevant endpoint, we chose to examine lesional fibrous cap thickness in response to LDL lowering ("atherosclerosis regression"). In humans, marked LDL lowering promotes fibrous cap thickening, which is a marker of low-risk, stable plaques (58), and a lower risk of CVD events (24-27). Importantly, activation of efferocytosis-resolution pathways in regressing lesional macrophages, including EIMP, plays a key role in cap thickening after LDL lowering (6, 7, 9, 28).

Accordingly, one group of irradiated *Ldlr*$^{-/-}$ mice, referred to as "chimeric RH", were transplanted with 20% bone marrow cells from GFP^{-} *Dnmt3a*^{R878H}*Csf1rCre*$^{Esr1+}$ mice (tamoxifen-inducible DNMT3A-RH) and 80% bone marrow cells from GFP+ C57BL/6J WT mice. Another group of mice, referred to as "WT RH", were transplanted with 20% bone marrow cells from GFP^{-} *Csf1rCre*$^{Esr1+}$ mice (DNMT3A-WT) and 80% bone marrow cells from GFP+ C57BL/6J WT mice. After 4 weeks of recovery, all mice were treated with tamoxifen to promote expression of *Dnmt3a*^{R878H} in the *Dnmt3a*^{R878H}*Csf1rCre*$^{Esr1+}$ cells in the chimeric RH cohort. The mice were then fed the Western diet for 17 weeks. Some of the mice were harvested (baseline), while others were subjected to LDL lowering for 6 weeks by switching to chow diet and injecting an antisense oligonucleotide targeting apolipoprotein B100 (apoB ASO) to induce regression (28) (**Supplemental Figure 6A**). As designed, the combination of chow diet and apoB ASO markedly lowered plasma cholesterol, and it was similar in the two cohorts (**Supplemental Figure 6B**). The regression cohorts had lower body weights, as expected (6, 7, 9), but they were similar in chimeric RH and WT mice (**Supplemental Figure 6C**). Peripheral blood cell counts were similar across all cohorts except for a modest lowering of white blood cells (WBCs) in chimeric RH versus WT regression mice (**Supplemental Figure 6D**). There was only a modest increase in the percentage of GFP^{-} RH cells in the chimeric RH mice as compared to GFP^{-} WT cells in the chimeric WT mice (**Supplemental Figure 6E**), which is consistent with a less pronounced expansion of peripheral white blood cells in humans with DNMT3A-CH compared with other CH variants (59).

Lesional analysis revealed that nuclear 8-OHdG in lesional macrophages was lower in regressing versus baseline lesions in the WT cohort (**Figure 6A, groups 3 versus 1**), consistent with increased macrophage

efferocytosis in regression and our finding here that efferocytosis lowers oxDNA (6, 7, 9, 28). In contrast, macrophage nuclear 8-OHdG was not decreased in the regressing lesions of chimeric RH mice (**Figure 6A, groups 4 versus 2**). Nuclear 8-OHdG levels in non-Mac2 regions did not differ significantly between WT and RH regression lesions (**Supplementary Figure 6F**), supporting a predominantly macrophage-associated effect. Consistent with our findings related to the DNA repair pathway shown in vitro and in the DEX-thymus model, nuclear PARP1 and MTH1 in lesional macrophages were elevated in regressing versus baseline WT lesions but not RH lesions (**Figure 6, B and C**). With regard to EIMP, while total lesional macrophages decrease in regression as shown previously (60) and here (**Supplemental Figure 6G**), the pro-resolving efferocytic macrophage subpopulation increases due to EIMP (7). We now demonstrate that this increase was blunted in chimeric RH regressing lesions (**Figure 6D**). In 6-week regressing lesions, the ratio of macrophage-associated versus free TUNEL$^+$ cells largely reflects continuing efferocytosis (6-9, 14), and we found that this pro-resolving endpoint was markedly decreased in chimeric RH versus WT regressing lesions (**Figure 6E**).

To further assess the presence of pro-resolving macrophage features during regression, we examined the expression of the pro-resolving markers TGF-β1 and arginase 1 within plaque macrophages. In chimeric WT mice, both markers were increased during regression compared with baseline. In contrast, TGF-β1 was not increased during regression in chimeric RH mice, while arginase 1 was increased in chimeric RH regression but not to the level in chimeric WT regressing lesions (**Supplementary Figure 7, A and B**). These data are consistent with our previous finding that EIMP expands the pool of macrophages that are particularly adept at carrying out continuing efferocytosis (7). Another marker of a pro-resolving environment is an increase FoxP3$^+$ regulatory T cells (61), which can interact with macrophages to promote efferocytosis, including in the setting of atherosclerosis regression (28, 62). In this context, the FoxP3+/CD3+ T cell ratio was increased in regressing chimeric WT lesions versus baseline, whereas this increase was not observed in chimeric RH lesions (**Supplementary Figure 7C**).

Finally, the most important human-relevant endpoint of LDL-lowering-induced atherosclerosis regression is fibrous cap thickening. We found that regression-induced cap thickening, clearly evident in the WT cohort, was markedly abrogated in the chimeric RH cohort (**Figure 6F**). The effect of chimeric RH in cap thickness in regression could not be explained by overall changes in non-cap lesion area or necrotic area, as although both parameters showed modest trends towards lower values in regression versus baseline, there were no differences between WT and chimeric mice in these endpoints at either baseline or during regression (**Supplemental Figure 7, D and E**). Moreover, cap-localized lumican-positive cells, which are collagen-producing cells that contribute to fibrous cap formation (63), were increased in chimeric WT regression lesions versus baseline, and this increase was blunted in chimeric RH mice (**Supplementary Figure 7C**). Thus, in an experimental model of DNMT3A-CH, the PARP1/MTH1 oxDNA repair pathway and its pro-resolving effects, notably EIMP, are impaired in the setting of LDL-lowering-induced plaque stabilization.

Although comparing regressing versus progressing lesions from humans is not feasible due to the lack of availability of plaque material obtained after LDL lowering, we were able to compare stable versus unstable regions of individual human carotid plaques obtained from 10 subjects who underwent clinically indicated carotid endarterectomies. As we published previously, the unstable regions of plaques have more lesional necrosis, less fibrosis, and a lower content of pro-resolving, pro-efferocytic mediators than the stable regions (64). Here, we show that lesional macrophages in the unstable regions have, on average, higher nuclear 8-OHdG and lower nuclear PARP1 and MTH1 than macrophages in stable regions (**Figure 6G and Supplemental Figure 8, A and B**). Notably, linear regression analysis revealed significant inverse correlations between nuclear 8-OHdG and both PARP1 and MTH1 levels in carotid plaque macrophages (**Figure 6H**). These data show an association between unstable plaques and decreased biochemical markers of the PARP1/MTH1 oxDNA repair pathway in humans.

Discussion

Efferocytosis reprograms macrophages to be pro-resolving through a variety of upstream pathways triggered by efferocytosis receptor signaling, changes in macrophage energy metabolism, and/or molecules derived from the phagolysosomal degradation of ACs, including methionine and nucleotides (6-9, 12-15). These pathways induce downstream pro-resolving processes, including IL-10 and TGF–β1 production, continuing efferocytosis, and pro-resolving macrophage proliferation (EIMP) (6-9, 12-15). In previous studies, links between the upstream triggers and the downstream resolution endpoints have involved cytoplasmic pathways that alter gene expression, post-translational protein modification, or cytoskeletal remodeling. Here we introduce what we believe to be a new mechanism involving DNA repair, which links an upstream AC-derived molecule (methionine) to a key resolution endpoint (EIMP).

EIMP requires multiple inputs to ensure activation of cell proliferation only in the setting of abundant ACs (7, 15-22). Previously described efferocytic inputs required for EIMP include receptor-mediated signaling through the efferocytosis receptor MerTK, nucleotides released from AC phagolysosomal degradation (7), and lactate released by enhanced macrophage glycolysis supporting MYC protein stabilization (15). The work here introduces suppression of oxDNA as a prerequisite checkpoint for EIMP. Moreover, our study uncovers that the AC-methionine/DNMT3A pathway initiates more than one pro-resolving action, as we showed previously that it represses the expression of ERK phosphatase DUSP4, enabling the expression of two pro-resolving mediators, prostaglandin E_2 and TGF-β1 (8).

The finding that efferocytosis-induced suppression of oxDNA requires DNMT3A has potentially important implications, as DNMT3A is the most common gene mutated in CH (65, 66). Based upon the findings here and in previous studies (7, 8, 28, 62), we propose that the failure of DNMT3A-mediated oxDNA suppression, which leads to defects in EIMP and is associated with lower levels of $Arg1^+$ macrophages, TGF-β1, and

regulatory T cells, contributes to disease processes linked to DNMT3A-CH, notably atherosclerosis (29-38). Other diseases associated with DNMT3A-CH that, in theory, could also involve this mechanism include heart failure (67) and aortic valvular stenosis (68), both of which are associated with changes regulatory T cells (68, 69), as well as osteoporosis (70), neurodegenerative disease (71, 72), metabolic disease (73), and non-hematologic malignancies (74). Given that DNMT3A-CH is a disease of aging (75) and that BER function declines with age (76), the defect in BER-mediated suppression of oxDNA in efferocytosing macrophages may be particularly pronounced in the aged population with DNMT3A-CH. Impaired tissue resolution is likely additive with other pathogenic consequences of DNMT3A-CH. For example, previous work unrelated to efferocytosis/resolution has shown that loss of DNMT3A function in macrophages activates pro-inflammatory pathways that accelerate osteoporosis and atherosclerosis progression (70, 77). In the osteoporosis study (70), impaired DNA methylation in DNMT3A-deficient macrophages was linked to increased binding of the pro-inflammatory transcription factors IRF3 and RelA to DNA. The atherosclerosis study (77) also suggested an inflammatory signature in DNMT3A-mutant macrophages. In particular, atherosclerotic lesions of *Ldlr*$^{-/-}$ mice transplanted with chimeric DNMT3A-KO bone marrow and fed a high-fat/high-cholesterol diet revealed a distinct adventitial macrophage population that had features of tissue resident macrophage but with an inflammatory cytokine profile (52).

For our chimeric DNMT3A-CH experiment, we used bone marrow cells harboring the human-like R878H mutation (R882H in humans), which is a potent loss-of-function CH mutation in the methyltransferase domain (35, 57). The use of this particular mutant is important for two reasons. First, although DNMT3A can have non-canonical functions in cells that do not involve DNA methylation (43), the DNMT3A pathways that macrophages use to link efferocytosis to resolution involve DNA methylation (Ref. (8) and here), which highlights the importance of the methyltransferase domain of DNMT3A in these processes. Second and most importantly, evidence is emerging that humans with this mutation, which is in the methylase domain and acts in a dominant-negative manner (78, 79), have the highest risk of cardiovascular disease among DNMT3A-CH individuals (35, 38, 40). Indeed, while there are some human studies that have failed to show a link between DNMT3A-CH and cardiovascular disease, the cohorts used in these studies may have included a large number of people with other types of DNMT3A-CH mutations, particularly in non-methyltransferase regions of DNMT3A (35). Moreover, an important recent study has raised the possibility that a lack of deep sequencing in previous DNMT3A-CH cardiovascular studies could have led to false-negative results (80).

Our area of focus in atherosclerosis has been on the role of pro-resolving efferocytic macrophages in promoting fibrous cap thickening (6-9), a key tissue resolution process strongly associated with decreased risk of acute atherosclerotic cardiovascular events in humans (81). In this study, we examined a critical, clinically relevant process known as "atherosclerosis regression," in which plaques develop thicker fibrous caps in response to marked LDL lowering (24-27). We and others have shown previously that fibrous cap thickening in regression requires efferocytosis-induced tissue resolution (2, 6, 7, 9, 23, 28, 82). Here, we

discovered that the regressing lesions of chimeric DNMT3A-CH mice had thinner fibrous caps and decreased numbers of cap-localized lumican$^+$ cells, which contribute to cap formation (63), along with evidence of impaired PARP1/MTH1-mediated oxDNA repair and defective EIMP. EIMP leads to an increase in the number of pro-resolving macrophages that can make TGF-β1 (7), and the aforementioned DNMT3A-DUSP4-ERK pathway leads directly to an increase in the synthesis and secretion of TGF-β1 in macrophages (8). As TGF-β1 is a pro-fibrotic factor involved in fibrous cap thickening (83), these two DNMT3A pathways provide a possible mechanistic link between loss of DNMT3A function in CH and the development of unstable human plaques. Indeed, we show here that thin-capped unstable human plaques have higher levels of 8-OHdG and lower nuclear PARP1 and MTH1 in lesional macrophages compared with more stable lesions. Moreover, linear regression analysis revealed significant inverse correlations between nuclear 8-OHdG and both PARP1 and MTH1 in carotid plaque macrophages. Interestingly, previous work has shown that urinary 8-OHdG levels are associated with cardiovascular events in humans (84, 85). Moving forward, we aim to compare features of plaque stability in atheroma specimens from people with and without DNMT3A-CH methyltransferase mutations. In particular, we predict that the lesions of DNMT3A-CH individuals, particularly those with mutations in methyltransferase domain (above), would have higher lesional oxDNA, impaired proliferation of pro-resolving macrophages, and thinner fibrous caps. Another future goal will be to integrate our findings related to atherosclerosis fibrous cap thinning in DNMT3A-CH with other settings in which DNMT3A-CH affects tissue fibrosis. For example, a previous study showed a link between DNMT3A-CH and pathological fibrosis in the heart, with a mechanism related to cardiac fibroblast activation (69). Thus, it will be interesting to understand how DNMT3A-CH prevents beneficial activation of fibroblast-like cells in atherosclerosis while enhancing pathologic cardiac fibroblast activation in fibrotic heart disease.

Another future goal is to determine the precise molecular mechanism linking DNMT3A-mediated DNA methylation to the PARP1/MTH1 oxDNA repair pathway. Our data suggest that the key downstream event is chromatin binding of PARP1 and nuclear localization of MTH1. One possibility is that the methylation at specific genomic regions, perhaps by altering gene expression, activates one or more processes that lead to the nuclear recruitment of DNA repair enzymes. However, the rapid suppression of 8-OHdG following AC uptake may point to a non-transcriptional mechanism, albeit still dependent on DNA methylation. For example, DNMT3A-mediated DNA methylation could alter overall chromatin architecture (86) in a way that promotes the rapid chromatin binding of PARP1 after efferocytosis. Additional future goals include understanding how the repair and hydrolysis of 8-OHdG license macrophages for proliferation after efferocytosis and, conversely, identifying the mechanism of cell cycle blockade when oxDNA repair is impaired due to DNMT3A LoF. Moreover, we are interested in exploring other consequences of DNMT3A-dependent PARP1 chromatin binding in efferocytosing macrophages, e.g., in the regulation of gene expression (87). Finally, future studies using temporal macrophage-Mth1 deletion in our preclinical mouse models will further define the DNMT3A-mediated BER pathway in vivo and help define potential therapeutic strategies for DNMT3A-CH diseases.

In summary, this study uncovers an efferocytosis-induced tissue resolution mechanism involving the activation of a BER-mediated oxDNA repair pathway. We propose that this pathway could be highly relevant to the hundreds of millions of people on LDL-lowering medications, as such therapy promotes plaque stabilization through mechanisms linked to efferocytosis-induced resolution (6, 7, 9, 28). The finding that the oxDNA repair pathway requires DNMT3A-mediated DNA methylation provides a mechanistic link between DNMT3A-CH and atherosclerotic CVD. Thus, a key question moving forward is if humans with methyltransferase-defective DNMT3A-CH exhibit impaired regression in response to LDL lowering due to defective efferocytosis-resolution pathways in lesional macrophages, including suppression of oxDNA and impaired EIMP. The answers to these questions have potentially impactful therapeutic implications given the growth of preclinical work examining ways to boost efferocytosis and resolution for atherosclerosis and other chronic inflammatory diseases driven by impaired efferocytosis and tissue resolution (88-94).

Methods

Sex as a biological variable. The in vivo experiments in this study used male mice. Most of the in vitro studies used bone marrow-derived macrophages (BMDMs) from male mice, but the efferocytosis-induced 8-OHdG suppression finding was confirmed in BMDMs from female mice. Human monocyte-derived macrophage (HMDMs) studies were made from blood monocytes of anonymous healthy adult donors whose sex was unidentified (New York Blood Center). Human carotid endarterectomy specimens (below) were from both female (21%) and male (79%) subjects. Although sex was not analyzed as an independent variable, we expect that the key findings in this study will be relevant in both males and females.

Statistics. GraphPad Prism software (v.10) was used for all statistical analyses. Data were tested for normality using either the D'Agostino-Pearson or the Shapiro–Wilk test. Data that passed the normality test were analyzed using the two-tailed Student's t-test for comparison of two groups or one-way analysis of variance (ANOVA) with Fisher's Least Significant Difference (LSD) post-hoc analysis for comparison of more than two groups. Data that were not normally distributed were analyzed using the Mann-Whitney test or the Kruskal-Wallis test. Data are shown as mean values ± S.E.M. and differences were considered statistically significant at $P < 0.05$. N-number for in vitro experiments refers to the number of wells of macrophages, n-number for the mouse experiments refers to the number of mice. For normalization of data, all values were divided by the means of the control group. No data were excluded.

Study approval. The Columbia University's Institutional Review Board and Health Insurance Portability and Accountability Act guidelines were followed for isolating peripheral human blood leukocytes. Mouse protocols were approved by Columbia University's Institutional Animal Care and Use Committee. All mice were cared for according to the NIH guidelines for the care and use of laboratory animals, and all were in good general health based on appearance and activity. The use of de-identified carotid artery specimens,

which were removed for clinical indications only and would otherwise have been discarded, conformed with the declaration of Helsinki and were approved for use by the Johannes Gutenberg University ethics review board. Informed written consent was obtained from each patient. The Columbia University IRB provided ethical approval for these studies, and procedures were conducted in accordance with an approved IRB protocol.

Data availability. Values for all data points in the graphs are reported in the Supporting Data Values file.

Additional detailed methods can be found in the Supplemental Methods.

Author contributions

KA and IT conceived and designed the research. KA conducted the experiments and collected and analyzed the data. DN, SRS, PA, JR, HZ, JG, and AV provided critical advice during the course of the project. BD donated patient samples, and BD, HW, and LM were instrumental in the interpretation of the human data. KA and IT wrote the manuscript, with comments provided by all other authors.

Conflict of interest

The authors have declared that no conflict of interest exists for this study.

Funding support

This work is the result of NIH funding, in whole or in part, and is subject to the NIH Public Access Policy. Through acceptance of this federal funding, the NIH has been given a right to make the work publicly available in PubMed Central. The content of this work is solely the responsibility of the authors and does not necessarily represent the official views of the NIH.

- R35-HL145228 to IT
- K99-HL181285 to SRS
- P01-HL172741 to IT
- American Heart Association Postdoctoral Fellowship Award to DN
- Translational Immunology Core Facility by P30CA013696, S10RR027050 and S10OD020056.
- Molecular Pathology Shared Resource of the Herbert Irving Comprehensive Cancer Center at Columbia University, by P30CA013696.

Acknowledgments

The authors thank Dr. Benjamin Ebert, Dana-Farber Cancer Institute, Harvard Medical School, for donating the *Dnmt3a*$^{fl/fl}$ *Vav1Cre*$^{+/-}$ and *Vav1Cre*$^{+/-}$ control mice for this study.

Figure Legends

Figure 1. Efferocytosis induces suppression of oxidized DNA in a DNMT3A-dependent manner. (**A**) BMDMs from wild-type (Ctrl) or *Dnmt3a*$^{-/-}$ (KO) mice were incubated without or with ACs (-ACs, +ACs) for 45 minutes, after which non-internalized ACs were removed by rinsing. After an additional 1-hour incubation, the cells were immunostained for 8-OHdG and histone 2A (H2A; nucleus), and 8-OHdG mean fluorescent intensity (MFI) in H2A-positive areas (arrows) was quantified by confocal fluorescence microscopy (*n* = 3 replicates/group; similar results were observed in 3 replicate experiments). (**B**) Similar to (A), but BMDMs were immunostained for the nuclear envelope marker lamin B, and 8-OHdG MFI inside lamin B-stained nuclei (arrows) was quantified (*n* = 3-4 replicates/group). (**C**) Similar to (A), but human monocyte-derived macrophages (HMDMs) were treated with scrambled RNA (Scr) or siDNMT3A, and 8-OHdG MFI in DAPI^{+} nuclei (arrows) was quantified (*n* = 4-6 replicates/group). (**D**) Similar to (A), but BMDMs were exposed to apoptotic HMDMs and quantified for 8-OHdG MFI in DAPI^{+} nuclei (arrows) (*n* = 3 replicates/group). (**E**) Control or DNMT3A-KO BMDMs were pretreated for 2 hours with vehicle (DMSO) or 20 μM 5-azacytidine (5-AzaC) and then quantified for 8-OHdG MFI in DAPI^{+} areas (arrows) (*n* = 3-4 replicates/group). (**F**) Mouse bone marrow stem cells were transduced with control or Tet1 retrovirus (Ctrl, or Tet1 RV) and then incubated for 7 days with M-CSF-containing macrophage differentiation medium. The resulting macrophages were quantified for 8-OHdG MFI in DAPI^{+} nuclei (*n* = 3 replicates/group). Arrows indicate nuclei. Scale bars, 50 μm. Data are mean ± s.e.m., and *P* values were determined by two-way ANOVA for panels A-D, and F and one-way ANOVA for panel E, with Fisher's LSD post-hoc analysis. **P* < 0.05; ***P* < 0.01; ****P* < 0.001; ****P < 0.0001; ns, non-significant.

Figure 2. Efferocytosis-induced suppression of oxDNA is dependent on PARP1. (**A**) BMDMs pre-treated with scrambled (Scr) or siOgg1 were incubated ± ACs for 45 minutes, rinsed, and incubated for an additional hour. The cells were immunostained for 8-OHdG and quantified for 8-OHdG MFI in DAPI^{+} areas (*n* = 3 replicates/group). Arrows, nuclei. (**B**) BMDMs were incubated ± ACs for 45 minutes, rinsed, and incubated for an additional hour. The cells were immunostained for PARP1 and quantified for PARP1 MFI in DAPI^{+} areas (*n* = 6 replicates/group). Arrows, nuclei. (**C**) As in (A), but the BMDMs were pre-treated with scrambled (Scr) or siParp1. (**D**) As in (A), but the BMDMs were pre-treated for 2 hours with vehicle (DMSO) or 20 μM PJ34. (**E**) As in (D), except HMDMs were used. (**F**) Control or DNMT3A-KO BMDMs were incubated ± ACs for 45 minutes, rinsed, and incubated for an additional hour. Chromatin fractions were immunoblotted for PARP1, poly-mono-ADP ribose, and histone 3 and quantified for the density-ratio of PARP1:histone 3 and PARylated protein:histone 3 (*n* = 3 replicates/group). (**G**) Wild-type (Control) or DNMT3A-KO BMDMs were pretreated for 2 hours with vehicle (DMSO) or 20 μM 5-azacytidine (5-AzaC) and then incubated ± ACs as in (F).

Chromatin fractions were immunoblotted for PARP1 and histone 3 and quantified for the PARP1:histone 3 ratio (n = 3 replicates/group). (**H**) Macrophages transduced with control or Tet1 retrovirus (Ctrl or Tet1 RV) were incubated ± ACs as in Figure 1F and quantified for PARP1 in DAPI$^+$ areas (n = 3 replicates/group). Scale bars, 50 μm. Data are mean ± s.e.m., and P values were determined by two-way ANOVA for panels A-F, and H) or one-way ANOVA for panel G, with Fisher's LSD post-hoc analysis. *P < 0.05; **P < 0.01; ***P < 0.001; ****P < 0.0001; ns, non-significant.

Figure 3. Efferocytosis-induced suppression of oxDNA is dependent on MTH1. (**A**) BMDMs were incubated ± ACs for 45 minutes, rinsed, and incubated for an additional hour. The cells were immunostained for MTH1 and stained with DAPI (nucleus) and then quantified for MTH1 MFI in DAPI$^+$ areas (n = 3-5 replicates/group). Arrows, nuclei. (**B**) Control or DNMT3A-KO BMDMs were incubated ± ACs for 45 minutes, rinsed, and incubated for an additional hour. The nuclear soluble fraction was immunoblotted for MTH1 and lamin B1 and quantified for the MTH1:lamin B1 ratio (n = 3 replicates/group). (**C**) Similar to (B), but with HMDMs (n = 3 replicates/group). (**D**) As in (A), but the macrophages were pretreated with scrambled (Scr) or siNudt1 (gene for MTH1), immunostained for 8-OHdG, and quantified for 8-OHdG MFI in DAPI$^+$ areas (n = 3 replicates/group). Arrows, nuclei. (**E**) Similar to (D), except the cells were pretreated for 2 hours with vehicle (DMSO) or 20 μM TH287. The cells were quantified for 8-OHdG MFI in DAPI$^+$ areas (arrows) (n = 3 replicates/group). (**F**) As in (B), but the control and DNMT3A-KO BMDMs were pretreated for 2 hours with vehicle (DMSO) or 20 μM 5-azacytidine (5-AzaC). The nuclear soluble fraction was immunoblotted for MTH1 and lamin B1 and quantified for the ratio of MTH1:lamin B1 (n = 3 replicates/group). (**G**) Macrophages transduced with Ctrl or Tet 1 RV were prepared as in Figure 1F and quantified for MTH1 MFI in DAPI$^+$ area (n = 3 replicates/group). (**H**) As in (D), except that the DNMT3A-KO macrophages were transduced with control or MTH1 retrovirus (Ctrl or MTH1 RV). The cells were quantified for 8-OHdG in DAPI$^+$ areas (arrows) (n = 5 replicates/group). Scale bars, 50 μm. Data are mean ± s.e.m., and P values were determined by two-way ANOVA for panels A-E and G-H) or one-way ANOVA for panel F, with Fisher's LSD post-hoc analysis. *P < 0.05; **P < 0.01; ***P < 0.001; ns, non-significant.

Figure 4. Efferocytosis-induced suppression of oxDNA is required for efferocytosis-induced macrophage proliferation (EIMP). (**A**) BMDMs from control or DNMT3A-KO mice were incubated ± ACs for 45 minutes, rinsed, and incubated for an additional 24 hours. Cell number was quantified (n = 3 replicates/group). (**B**) Similar to (A), but the percentage of Ki67$^+$ macrophages or EdU$^+$ macrophages (after a 2-hour pretreatment with 20 μM EdU) was quantified using immunofluorescence microscopy (n = 3-4 replicates/group). (**C**) Similar to (B), but the percentage of p21$^+$ macrophages was quantified (n = 3 replicates/group). (**D**) Control or DNMT3A-KO BMDMs were pretreated for 2 hours with 20 μM PJ34, TH287, or vehicle control (DMSO). The cells were incubated ± ACs for 45 minutes, rinsed, incubated for an additional

24 hours, and quantified for cell number (*n* = 3 replicates/group). (**E**) Similar to (D), but the percentage of Ki67$^+$ macrophages was quantified (*n* = 3 replicates/group). (**F**) HMDMs pretreated with 20 μM PJ34 or vehicle control (DMSO) were incubated ± ACs for 45 minutes, rinsed, and incubated for an additional 24 hours. The percentage of Ki67$^+$ macrophages was quantified (*n* = 4 replicates/group). (**G**) DNMT3A-KO macrophages were retrovirally with control or MTH1 RV as in Figure 3H. The cells were incubated ± ACs for 45 minutes, rinsed, and incubated for an additional 24 hours, and quantified for the percentage of Ki67$^+$ macrophages or EdU$^+$ macrophages as in (B) (*n* = 3-4 replicates/group). Scale bars, 50 μm. Data are mean ± s.e.m., and *P* values were determined by the Student's t-test for panels B, C, F, and G, two-way ANOVA for panels A and D, and one-way ANOVA for panel E, with Fisher's LSD post-hoc analysis. *P < 0.05; **P < 0.01; ***P < 0.001; ****P < 0.0001.

Figure 5. Efferocytosis-induced suppression of oxDNA is required for tissue resolution *in vivo*. Mice were transplanted with bone marrow from control *Vav1cre*$^{+/-}$ (Ctrl) or *Dnmt3a*$^{fl/fl}$*Vav1cre*$^{+/-}$ (KO) mice. After 4 weeks, the mice were injected with PBS or dexamethasone (DEX), and the thymi were harvested after 4 or 18 hours. The 4-hour thymic sections were: (**A**) immunostained for Mac2 and DNMT3A and quantified for DNMT3A MFI in Mac2$^+$ areas (*n* = 7-8 mice/group) (**B**) quantified for the ratio of macrophage-associated:free TUNEL$^+$ cells (arrows) (*n* = 6 mice/group). (**C**) immunostained for Mac2 and 8-OHdG (arrows), stained with DAPI, and quantified for 8-OHdG MFI in Mac2$^+$DAPI$^+$ areas (*n* = 4-6 mice/group). (**D**) immunostained for Mac2 and PARP1 (arrows), stained with DAPI, and quantified as PARP1 MFI in Mac2$^+$DAPI$^+$ areas (*n* = 4-6 mice/group). (**E**) immunostained for Mac2 and MTH1 (arrows), stained with DAPI, and quantified as MTH1 MFI in Mac2$^+$DAPI$^+$ areas (*n* = 4-5 mice/group). (**F**) As in (C), but the mice were treated with 25 mg/kg PJ34, 5 mg/kg TH287, or vehicle (DMSO) 30 min before and 15 min and 2 hours after DEX (*n* = 5 mice/group). (**G**) 18-hour thymi of control or KO mice were immunostained for Mac2 and Ki67 (arrows), stained with DAPI, and quantified as the percent Ki67$^+$ macrophages/thymic macrophages (*n* = 7-8 mice/group). (**H-J**) C57BL/6J mice were treated with TH287 as in (F). After 18 hours, the thymic sections were: (**H**) quantified for the ratio of macrophage-associated:free TUNEL$^+$ cells (arrows). (**I**) immunostained for Mac2 and Ki67 (arrows), stained with DAPI, and quantified as the percent Ki67$^+$ macrophages/thymic macrophages. (**J**) H&E-stained were assayed for the percent necrotic areas (regions of hypocellularity and/or small, fragmented nuclei). For panels H-J, *n* = 7-8 mice/group. Scale bars, 50 μm. Data are mean ± s.e.m., and *P* values were determined by the Student's t-test for panels A-B and G-J, two-way ANOVA for panels C-E, or one-way ANOVA for panel F, with Fisher's LSD post-hoc analysis. *P < 0.05; **P < 0.01; ***P < 0.001; ****P < 0.0001; ns, non-significant.

Figure 6. Impaired efferocytosis-induced suppression of oxDNA in atherosclerosis regression in a model of DNMT3A clonal hematopoiesis. (**A-F**) *Ldlr*$^{-/-}$ mice were transplanted with a 20%/80% mixture of bone marrow cells from GFP$^-$ *Dnmt3a*^{R878H}*Csf1rCre*$^{Esr1+}$ mice and GFP$^+$ wild-type mice (Chimeric RH) or a

20%/80% mixture of bone marrow cells from GFP^- and GFP^+ wild-type mice (Chimeric WT). After 4 weeks, the mice were treated with tamoxifen to induce *Dnmt3a*^{R878H} and fed a Western-type diet for 17 weeks. Some mice were harvested (Baseline), while others were injected with apoB ASO and fed a chow diet for 5 weeks (Regression). The aortic root sections were: (**A**) immunostained for Mac2 and 8-OHdG (arrows), stained with DAPI, and quantified as 8-OHdG MFI (MFI) in $Mac2^+DAPI^+$ areas (*n* = 7-9 mice/group, with similar data in a replicate experiment). (**B**) immunostained for Mac2 and PARP1 (arrows), stained with DAPI, and quantified as PARP1 MFI in $Mac2^+DAPI^+$ areas (*n* = 7-9 mice/group). (**C**) immunostained for Mac2 and MTH1 (arrows) and stained with DAPI and quantified as MTH1 MFI in $Mac2^+DAPI^+$ areas (*n* = 7-9 mice/group). (**D**) immunostained for Mac2 and Ki67 (arrows), stained with DAPI, and quantified as the percent $Ki67^+$ macrophages (*n* = 7-8 mice/group). (**E**) assayed for the ratio of macrophage-associated:free $TUNEL^+$ cells (arrows) (*n* = 7 mice/group). (**F**) stained with Sirius red and assayed for fibrous cap thickness (arrows), expressed relative to the WT baseline group (*n* = 9 mice/group). Scale bar, 50 μm. (**G**) Stable and unstable regions of human carotid endarterectomy specimens were immunostained for 8-OHdG, PARP1, and MTH1 and quantified as 8-OHdG, PARP1, or MTH1 MFI in $CD68^+DAPI^+$ areas (*n* = 10 human specimens). (**H**) Regression analyses of the correlations between macrophage 8-OHdG and PARP1 (left) or MTH1 (right) based on the data in (G). Scale bars, 50 μm. Data in panels A-G are mean ± s.e.m., and *P* values were determined by two-way ANOVA with Fisher's LSD post-hoc analysis for panels A-D, and F or the Student's t-test for panels E and G. **P* < 0.05; ***P* < 0.01; ***P < 0.001; ****P < 0.0001; ns, non-significant. R^2 and P-values are shown in panel H.

1. Morioka S, Maueroder C, and Ravichandran KS. Living on the edge: Efferocytosis at the interface of homeostasis and pathology. *Immunity.* 2019;50(5):1149–62.
2. Doran AC, Yurdagul A, Jr., and Tabas I. Efferocytosis in health and disease. *Nat Rev Immunol.* 2020;20(4):254–67.
3. Boada-Romero E, Martinez J, Heckmann BL, and Green DR. The clearance of dead cells by efferocytosis. *Nat Rev Mol Cell Biol.* 2020;21(7):398–414.
4. Park D, Han CZ, Elliott MR, Kinchen JM, Trampont PC, Das S, et al. Continued clearance of apoptotic cells critically depends on the phagocyte Ucp2 protein. *Nature.* 2011;477(7363):220–4.
5. Wang Y, Subramanian M, Yurdagul A, Jr., Barbosa-Lorenzi VC, Cai B, de Juan-Sanz J, et al. Mitochondrial fission promotes the continued clearance of apoptotic cells by macrophages. *Cell.* 2017;171(2):331–45 e22.
6. Yurdagul A, Jr., Subramanian M, Wang X, Crown SB, Ilkayeva OR, Darville L, et al. Macrophage metabolism of apoptotic cell-derived arginine promotes continual efferocytosis and resolution of injury. *Cell Metab.* 2020;31(3):518–33 e10.
7. Gerlach BD, Ampomah PB, Yurdagul A, Jr., Liu C, Lauring MC, Wang X, et al. Efferocytosis induces macrophage proliferation to help resolve tissue injury. *Cell Metab.* 2021;33(12):2445–63 e8.
8. Ampomah PB, Cai B, Sukka SR, Gerlach BD, Yurdagul A, Jr., Wang X, et al. Macrophages use apoptotic cell-derived methionine and DNMT3A during efferocytosis to promote tissue resolution. *Nat Metab.* 2022;4(4):444–57.
9. Sukka SR, Ampomah PB, Darville LNF, Ngai D, Wang X, Kuriakose G, et al. Efferocytosis drives a tryptophan metabolism pathway in macrophages to promote tissue resolution. *Nat Metab.* 2024;6(9):1736–55.
10. Dalli J, and Serhan CN. Pro-resolving mediators in regulating and conferring macrophage function. *Front Immunol.* 2017;8:1400.
11. McDonald PP, Fadok VA, Bratton D, and Henson PM. Transcriptional and translational regulation of inflammatory mediator production by endogenous TGF-beta in macrophages that have ingested apoptotic cells. *J Immunol.* 1999;163(11):6164–72.
12. Zhang S, Weinberg S, DeBerge M, Gainullina A, Schipma M, Kinchen JM, et al. Efferocytosis fuels requirements of fatty acid oxidation and the electron transport chain to polarize macrophages for tissue repair. *Cell Metab.* 2018;29(2):443–56 e5.
13. Morioka S, Perry JSA, Raymond MH, Medina CB, Zhu Y, Zhao L, et al. Efferocytosis induces a novel SLC program to promote glucose uptake and lactate release. *Nature.* 2018;563(7733):714–8.
14. Schilperoort M, Ngai D, Katerelos M, Power DA, and Tabas I. PFKFB2-mediated glycolysis promotes lactate-driven continual efferocytosis by macrophages. *Nat Metab.* 2023;5(3):431–44.
15. Ngai D, Schilperoort M, and Tabas I. Efferocytosis-induced lactate enables the proliferation of pro-resolving macrophages to mediate tissue repair. *Nat Metab.* 2023;5(12):2206–19.
16. Jeelani I, Moon JS, da Cunha FF, Nasamran CA, Jeon S, Zhang X, et al. HIF-2α drives hepatic Kupffer cell death and proinflammatory recruited macrophage activation in nonalcoholic steatohepatitis. *Sci Transl Med.* 2024;16(764):eadi0284.
17. Zhang CR, Xiong L, Gu M, Yeh CY, Jerby L, Kundaje A, et al. Cancer cell phagocytosis induces an anti-inflammatory gene regulatory program in macrophages. *bioRxiv.* 2025.
18. Tu M, Zou X, Tan X, Liu Y, Ge X, Hu Y, et al. 4-octyl itaconate promotes diabetic wound healing by enhancing pro-resolving macrophages via the efferocytosis-MCT1-lactate-GPR132 pathway and macrophage-independent synergistic effects. *Diabetes Metab J.* 2025.
19. Liu Y, Xue R, Duan X, Shang X, Wang M, Wang F, et al. PARP inhibition synergizes with CD47 blockade to promote phagocytosis by tumor-associated macrophages in homologous recombination-proficient tumors. *Life Sci.* 2023;326:121790.
20. Zhang D, Wang X, Zhu L, Chen Y, Yang C, Zhong Z, et al. TIMD4(hi)MHCII(hi) macrophages preserve heart function through Retnla. *JACC Basic Transl Sci.* 2025;10(1):65–84.

21. Zeng L, Wang Y, Huang Y, Yang W, Zhou P, Wan Y, et al. IRG1/itaconate enhances efferocytosis by activating Nrf2-TIM4 signaling pathway to alleviate con A induced autoimmune liver injury. *Cell Commun Signal*. 2025;23(1):63.
22. Yin Z, Zhang J, Zhao M, Liu J, Xu Y, Peng S, et al. EDIL3/Del-1 prevents aortic dissection through enhancing internalization and degradation of apoptotic vascular smooth muscle cells. *Autophagy*. 2024;20(11):2405–25.
23. Fisher EA. Regression of atherosclerosis: The journey from the liver to the plaque and back. *Arterioscler Thromb Vasc Biol*. 2016;36(2):226–35.
24. Puri R, Nissen SE, Ballantyne CM, Barter PJ, Chapman MJ, Erbel R, et al. Factors underlying regression of coronary atheroma with potent statin therapy. *Eur Heart J*. 2013;34(24):1818–25.
25. Conte E, Perone F, Cosyns B, Dweck MR, Donal E, Goncalves I, et al. Therapies leading to coronary atherosclerosis plaque regression: a scientific statement of the European Association of Preventive Cardiology, the European Association of Cardiovascular Imaging of the ESC, the ESC Working Group on Atherosclerosis and Vascular Biology, and the ESC Working Group on Cardiovascular Pharmacotherapy Part 1: Atherosclerosis pathophysiology and imaging evaluation. *Eur J Prev Cardiol*. 2025.
26. Sipahi I, Nicholls SJ, Tuzcu EM, and Nissen SE. Coronary atherosclerosis can regress with very intensive statin therapy. *Cleve Clin J Med*. 2006;73(10):937–44.
27. Raber L, Ueki Y, Otsuka T, Losdat S, Haner JD, Lonborg J, et al. Effect of alirocumab added to high-intensity statin therapy on coronary atherosclerosis in patients with acute myocardial infarction: The PACMAN-AMI randomized clinical trial. *JAMA*. 2022;327(18):1771–81.
28. Sharma M, Schlegel MP, Afonso MS, Brown EJ, Rahman K, Weinstock A, et al. Regulatory T cells license macrophage pro-resolving functions during atherosclerosis regression. *Circ Res*. 2020;127(3):335–53.
29. Jaiswal S, Natarajan P, Silver AJ, Gibson CJ, Bick AG, Shvartz E, et al. Clonal hematopoiesis and risk of atherosclerotic cardiovascular disease. *N Engl J Med*. 2017;377(2):111–21.
30. Lee H, Song H, Choi SY, Koh Y, Ryu G, Park HE, et al. Impact of clonal haematopoiesis on atherosclerotic cardiovascular disease according to low-density lipoprotein cholesterol levels in general population. *Eur J Prev Cardiol*. 2024.
31. Gumuser ED, Schuermans A, Cho SMJ, Sporn ZA, Uddin MM, Paruchuri K, et al. Clonal hematopoiesis of indeterminate potential predicts adverse outcomes in patients with atherosclerotic cardiovascular disease. *J Am Coll Cardiol*. 2023;81(20):1996–2009.
32. Zhao K, Shen X, Liu H, Lin Z, Li J, Chen S, et al. Somatic and germline variants and coronary heart disease in a Chinese population. *JAMA Cardiol*. 2024.
33. Schuermans A, Nakao T, Ruan Y, Koyama S, Yu Z, Uddin MM, et al. Birth weight is associated with clonal hematopoiesis of indeterminate potential and cardiovascular outcomes in adulthood. *J Am Heart Assoc*. 2023;12(13):e030220.
34. Kislikova M, Lopez MAB, Salinas FJF, Blanco JAP, Molina MPG, Fernandez AA, et al. Clonal hematopoiesis of indeterminate potential and cardiovascular risk in patients with chronic kidney disease without previous cardiac pathology. *Life (Basel)*. 2023;13(9).
35. Silver AJ, Brown DJ, Vlasschaert C, Bhat P, Pusso F, Van Amburg JC, et al. DNMT3A R882H exhibits greater infammatory potential than R882C in primary hematopoietic stem and progenitor cell knock-in model and population data. *Blood*. 2023;142:815–7.
36. Zuo C, Fu D, Huang Y, Li J, Yang S, Cheng X, et al. Association of clonal hematopoiesis of indeterminate potential with cardiometabolic multimorbidity progression and mortality: a prospective study of UK Biobank. *Eur J Med Res*. 2025;30(1):414.
37. Xue L, Bhattacharya R, Uddin MM, Nakao T, Zou R, Patel A, et al. Clonal hematopoiesis and major adverse cardiac events in people with HIV: insights from the REPRIEVE trial. *Arterioscler Thromb Vasc Biol*. 2025.
38. Flynn S, Schuermans A, Uddin MM, Nakao T, Viscosi V, Libby P, et al. Clonal hematopoiesis and incident heart failure. *JAMA Cardiol*. 2025.

39. von Scheidt M, Adkar SS, Krefting J, Hoermann G, Meggendorfer M, Bauer S, et al. Clonal haematopoiesis of indeterminate potential and mortality in coronary artery disease. *Eur Heart J*. 2026;47(4):453–69.
40. Pershad Y, Zhao K, Van Amburg JC, Corty RW, Parker AC, Silver AJ, et al. Mutation-specific impairment of TET2 and DNMT3A enzymatic activity predicts clonal hematopoiesis disease risk. *medRxiv*. 2026.
41. Tabas I. Consequences and therapeutic implications of macrophage apoptosis in atherosclerosis: the importance of lesion stage and phagocytic efficiency. *Arterioscler Thromb Vasc Biol*. 2005;25(11):2255–64.
42. Okano M, Bell DW, Haber DA, and Li E. DNA methyltransferases Dnmt3a and Dnmt3b are essential for de novo methylation and mammalian development. *Cell*. 1999;99(3):247–57.
43. Xavier Raj I, Kyun Koh W, Harrison J, Zhang CR, Soares B, Amato R, et al. Non-canonical functions of DNMT3A in hematopoietic stem cells regulate telomerase activity and genome integrity. *Cell Stem Cell*. 2025.
44. Cobo I, Tanaka TN, Chandra Mangalhara K, Lana A, Yeang C, Han C, et al. DNA methyltransferase 3 alpha and TET methylcytosine dioxygenase 2 restrain mitochondrial DNA-mediated interferon signaling in macrophages. *Immunity*. 2022;55(8):1386–401 e10.
45. Hoang NM, Liu Y, Bates PD, Heaton AR, Lopez AF, Liu P, et al. Targeting DNMT3A-mediated oxidative phosphorylation to overcome ibrutinib resistance in mantle cell lymphoma. *Cell Rep Med*. 2024;5(4):101484.
46. Hegde ML, Hazra TK, and Mitra S. Early steps in the DNA base excision/single-strand interruption repair pathway in mammalian cells. *Cell Res*. 2008;18(1):27–47.
47. Ishibashi T, Hayakawa H, Ito R, Miyazawa M, Yamagata Y, and Sekiguchi M. Mammalian enzymes for preventing transcriptional errors caused by oxidative damage. *Nucleic Acids Res*. 2005;33(12):3779–84.
48. Abdelkarim GE, Gertz K, Harms C, Katchanov J, Dirnagl U, Szabó C, et al. Protective effects of PJ34, a novel, potent inhibitor of poly(ADP-ribose) polymerase (PARP) in in vitro and in vivo models of stroke. *Int J Mol Med*. 2001;7(3):255–60.
49. Muthurajan UM, Hepler MR, Hieb AR, Clark NJ, Kramer M, Yao T, et al. Automodification switches PARP-1 function from chromatin architectural protein to histone chaperone. *Proc Natl Acad Sci U S A*. 2014;111(35):12752–7.
50. Gad H, Koolmeister T, Jemth AS, Eshtad S, Jacques SA, Ström CE, et al. MTH1 inhibition eradicates cancer by preventing sanitation of the dNTP pool. *Nature*. 2014;508(7495):215–21.
51. Rai P, Onder TT, Young JJ, McFaline JL, Pang B, Dedon PC, et al. Continuous elimination of oxidized nucleotides is necessary to prevent rapid onset of cellular senescence. *Proc Natl Acad Sci U S A*. 2009;106(1):169–74.
52. Kinoshita A, Wanibuchi H, Imaoka S, Ogawa M, Masuda C, Morimura K, et al. Formation of 8-hydroxydeoxyguanosine and cell-cycle arrest in the rat liver via generation of oxidative stress by phenobarbital: association with expression profiles of p21(WAF1/Cip1), cyclin D1 and Ogg1. *Carcinogenesis*. 2002;23(2):341–9.
53. Lin Y, Waldman BC, and Waldman AS. Suppression of high-fidelity double-strand break repair in mammalian chromosomes by pifithrin-alpha, a chemical inhibitor of p53. *DNA Repair (Amst)*. 2003;2(1):1–11.
54. Matsuda T, Kato T, Kiyotani K, Tarhan YE, Saloura V, Chung S, et al. p53-independent p21 induction by MELK inhibition. *Oncotarget*. 2017;8(35):57938–47.
55. Squires S, Coates JA, Goldberg M, Toji LH, Jackson SP, Clarke DJ, et al. p53 prevents the accumulation of double-strand DNA breaks at stalled-replication forks induced by UV in human cells. *Cell Cycle*. 2004;3(12):1543–57.
56. Elliott MR, Chekeni FB, Trampont PC, Lazarowski ER, Kadl A, Walk SF, et al. Nucleotides released by apoptotic cells act as a find-me signal to promote phagocytic clearance. *Nature*. 2009;461(7261):282–6.

57. Cole CB, Russler-Germain DA, Ketkar S, Verdoni AM, Smith AM, Bangert CV, et al. Haploinsufficiency for DNA methyltransferase 3A predisposes hematopoietic cells to myeloid malignancies. *J Clin Invest*. 2017;127(10):3657–74.
58. Bentzon JF, Otsuka F, Virmani R, and Falk E. Mechanisms of plaque formation and rupture. *Circ Res*. 2014;114(12):1852–66.
59. Fabre MA, de Almeida JG, Fiorillo E, Mitchell E, Damaskou A, Rak J, et al. The longitudinal dynamics and natural history of clonal haematopoiesis. *Nature*. 2022;606(7913):335–42.
60. Feig JE, Vengrenyuk Y, Reiser V, Wu C, Statnikov A, Aliferis CF, et al. Regression of atherosclerosis is characterized by broad changes in the plaque macrophage transcriptome. *PLoS ONE*. 2012;7(6):e39790.
61. Josefowicz SZ, Lu LF, and Rudensky AY. Regulatory T cells: mechanisms of differentiation and function. *Annu Rev Immunol*. 2012;30:531–64.
62. Proto JD, Doran AC, Gusarova G, Yurdagul A, Jr., Sozen E, Subramanian M, et al. Regulatory T cells promote macrophage efferocytosis during inflammation resolution. *Immunity*. 2018;49(4):666–77.e6.
63. Onda M, Ishiwata T, Kawahara K, Wang R, Naito Z, and Sugisaki Y. Expression of lumican in thickened intima and smooth muscle cells in human coronary atherosclerosis. *Exp Mol Pathol*. 2002;72(2):142–9.
64. Fredman G, Hellmann J, Proto JD, Kuriakose G, Colas RA, Dorweiler B, et al. An imbalance between specialized pro-resolving lipid mediators and pro-inflammatory leukotrienes promotes instability of atherosclerotic plaques. *Nature Communications*. 2016;7:12859.
65. Yu Z, Fidler TP, Ruan Y, Vlasschaert C, Nakao T, Uddin MM, et al. Genetic modification of inflammation- and clonal hematopoiesis-associated cardiovascular risk. *J Clin Invest*. 2023;133(18):2022.12.08.22283237.
66. Bick AG, Weinstock JS, Nandakumar SK, Fulco CP, Bao EL, Zekavat SM, et al. Inherited causes of clonal haematopoiesis in 97,691 whole genomes. *Nature*. 2020;586(7831):763–8.
67. Dorsheimer L, Assmus B, Rasper T, Ortmann CA, Ecke A, Abou-El-Ardat K, et al. Association of mutations contributing to clonal hematopoiesis with prognosis in chronic ischemic heart failure. *JAMA Cardiol*. 2019;4(1):25–33.
68. Mas-Peiro S, Hoffmann J, Fichtlscherer S, Dorsheimer L, Rieger MA, Dimmeler S, et al. Clonal haematopoiesis in patients with degenerative aortic valve stenosis undergoing transcatheter aortic valve implantation. *Eur Heart J*. 2020;41(8):933–9.
69. Shumliakivska M, Luxán G, Hemmerling I, Scheller M, Li X, Müller-Tidow C, et al. DNMT3A clonal hematopoiesis-driver mutations induce cardiac fibrosis by paracrine activation of fibroblasts. *Nat Commun*. 2024;15(1):606.
70. Kim PG, Niroula A, Shkolnik V, McConkey M, Lin AE, Slabicki M, et al. Dnmt3a-mutated clonal hematopoiesis promotes osteoporosis. *J Exp Med*. 2021;218(12).
71. Choi J, Park KS, Le Guen Y, Park JH, Zhou Z, Enyenihi L, et al. Clonal hematopoiesis mutations increase risk of Alzheimer's disease with APOE ε3/ε3 genotype. *bioRxiv*. 2025.
72. Lee S, Kim HJ, Kim S, Jin B, Jeon H, Woo KA, et al. Clonal hematopoiesis with DNMT3A mutations is associated with multiple system atrophy. *Parkinsonism Relat Disord*. 2024;128:107145.
73. Yan B, Yuan Q, Kaur P, McKee AR, Shabashvili DE, and Guryanova OA. Clonal hematopoiesis driven by Dnmt3a mutations promotes metabolic disease development. *bioRxiv*. 2025.
74. Lai J, Xi Z, Zhu D, Zhang Q, Yang Y, Wang X, et al. Title: clonal hematopoiesis of indeterminate potential and the risk of breast cancer a UK Biobank cohort study. *Int J Surg*. 2025.
75. Jaiswal S, Fontanillas P, Flannick J, Manning A, Grauman PV, Mar BG, et al. Age-related clonal hematopoiesis associated with adverse outcomes. *N Engl J Med*. 2014;371(26):2488–98.
76. Cabelof DC, Raffoul JJ, Yanamadala S, Ganir C, Guo Z, and Heydari AR. Attenuation of DNA polymerase beta-dependent base excision repair and increased DMS-induced mutagenicity in aged mice. *Mutat Res*. 2002;500(1-2):135–45.

77. Rauch PJ, Gopakumar J, Silver AJ, Nachun D, Ahmad H, Mcconkey M, et al. Loss-of-function mutations in *Dnmt3a* and *Tet2* lead to accelerated atherosclerosis and concordant macrophage phenotypes. *Nature Cardiovascular Research*. 2023;2(9):805–18.
78. Russler-Germain DA, Spencer DH, Young MA, Lamprecht TL, Miller CA, Fulton R, et al. The R882H DNMT3A mutation associated with AML dominantly inhibits wild-type DNMT3A by blocking its ability to form active tetramers. *Cancer Cell*. 2014;25(4):442–54.
79. Garcia EM, Lavidor OR, Raval S, Lue NZ, Liang JK, McFadden M, et al. Genetic landscape of DNMT3A R882H reveals mechanism of aberrant oligomerization. *bioRxiv*. 2025.
80. Corty R, Pershad Y, Heimlich JB, Vlasschaert C, Luo L, Mack T, et al. Detection of clonal hematopoiesis of indeterminate potential via genome or exome sequencing underestimates disease associations. *J Clin Invest*. 2026;136(5).
81. Virmani R, Burke AP, Kolodgie FD, and Farb A. Pathology of the thin-cap fibroatheroma: a type of vulnerable plaque. *J Interv Cardiol*. 2003;16(3):267–72.
82. Yurdagul A, Jr., Kong N, Gerlach BD, Wang X, Ampomah P, Kuriakose G, et al. ODC (ornithine decarboxylase)-dependent putrescine synthesis maintains MerTK (MER tyrosine-protein kinase) expression to drive resolution. *Arterioscler Thromb Vasc Biol*. 2021;41(3):e144–e59.
83. Gomez D, and Owens GK. Smooth muscle cell phenotypic switching in atherosclerosis. *Cardiovasc Res*. 2012;95(2):156–64.
84. Di Minno A, Turnu L, Porro B, Squellerio I, Cavalca V, Tremoli E, et al. 8-hydroxy-2-deoxyguanosine levels and cardiovascular disease: a systematic review and meta-analysis of the literature. *Antioxid Redox Signal*. 2016;24(10):548–55.
85. Kroese LJ, and Scheffer PG. 8-hydroxy-2'-deoxyguanosine and cardiovascular disease: a systematic review. *Curr Atheroscler Rep*. 2014;16(11):452.
86. Li S, Peng Y, and Panchenko AR. DNA methylation: Precise modulation of chromatin structure and dynamics. *Curr Opin Struct Biol*. 2022;75:102430.
87. Huang D, and Kraus WL. The expanding universe of PARP1-mediated molecular and therapeutic mechanisms. *Mol Cell*. 2022;82(12):2315–34.
88. Mehrotra P, and Ravichandran KS. Drugging the efferocytosis process: concepts and opportunities. *Nat Rev Drug Discov*. 2022;21(8):601–20.
89. Serhan CN. Treating inflammation and infection in the 21st century: new hints from decoding resolution mediators and mechanisms. *Faseb j*. 2017;31(4):1273–88.
90. Fredman G, and Tabas I. Boosting inflammation resolution in atherosclerosis: the next frontier for therapy. *Am J Pathol*. 2017;187(6):1211–21.
91. Saas P, Vetter M, Maraux M, Bonnefoy F, and Perruche S. Resolution therapy: Harnessing efferocytic macrophages to trigger the resolution of inflammation. *Front Immunol*. 2022;13:1021413.
92. He Z, Luo Y, Duan Z, Su B, Zeng W, Guo Y, et al. IRF5 siRNA nanoimmunotherapy: restoring macrophage efferocytosis in atherosclerosis. *Circulation*. 2025;152(22):1564–81.
93. Dong X, Zhao X, Gao J, Bo L, Li C, Kong Z, et al. Synthetic cleavage-resistant TREM2 boosts macrophage efferocytosis to treat inflammatory diseases. *Cell Rep Med*. 2026;7(2):102580.
94. Kirtay M, Ispirjan M, Bonnard B, Bruggner AL, Boehringer L, Miessler M, et al. CD47 blockade reprograms the monocyte-macrophage axis to promote inflammation resolution in atherosclerosis. *bioRxiv*. 2026.

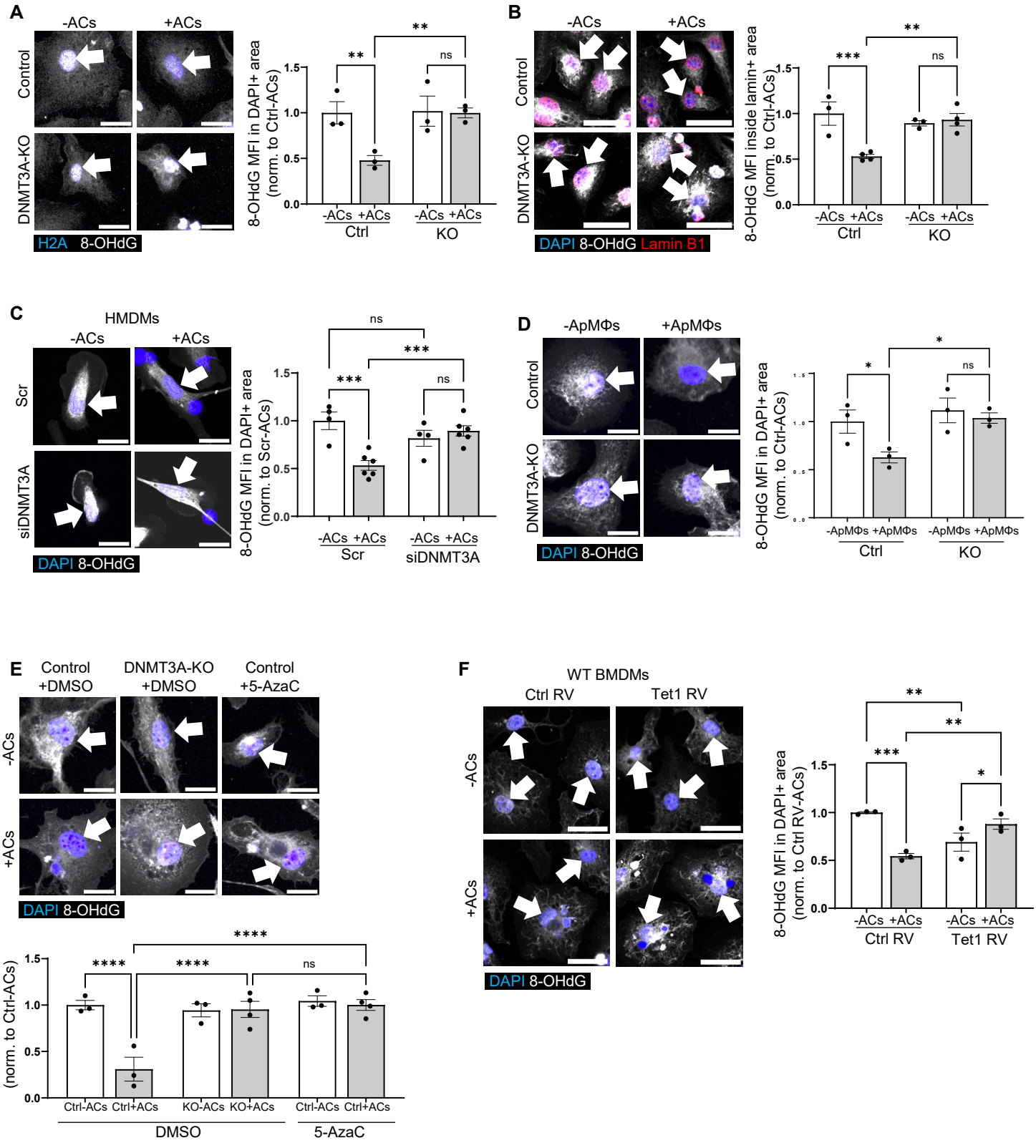
A
-ACs
+ACs
Control
DNMT3A-KO
H2A 8-OHdG
8-OHdG MFI in DAPI+ area (norm. to Ctrl-ACs)
Ctrl
KO
B
DAPI 8-OHdG Lamin B1
8-OHdG MFI inside lamin+ area (norm. to Ctrl-ACs)
C
HMDMs
Scr
siDNMT3A
DAPI 8-OHdG
8-OHdG MFI in DAPI+ area (norm. to Scr-ACs)
D
-ApMΦs
+ApMΦs
8-OHdG MFI in DAPI+ area (norm. to Ctrl-ACs)
E
Control +DMSO
DNMT3A-KO +DMSO
Control +5-AzaC
Ctrl-ACs Ctrl+ACs KO-ACs KO+ACs Ctrl-ACs Ctrl+ACs
DMSO
5-AzaC
F
WT BMDMs
Ctrl RV
Tet1 RV
8-OHdG MFI in DAPI+ area (norm. to Ctrl RV-ACs)

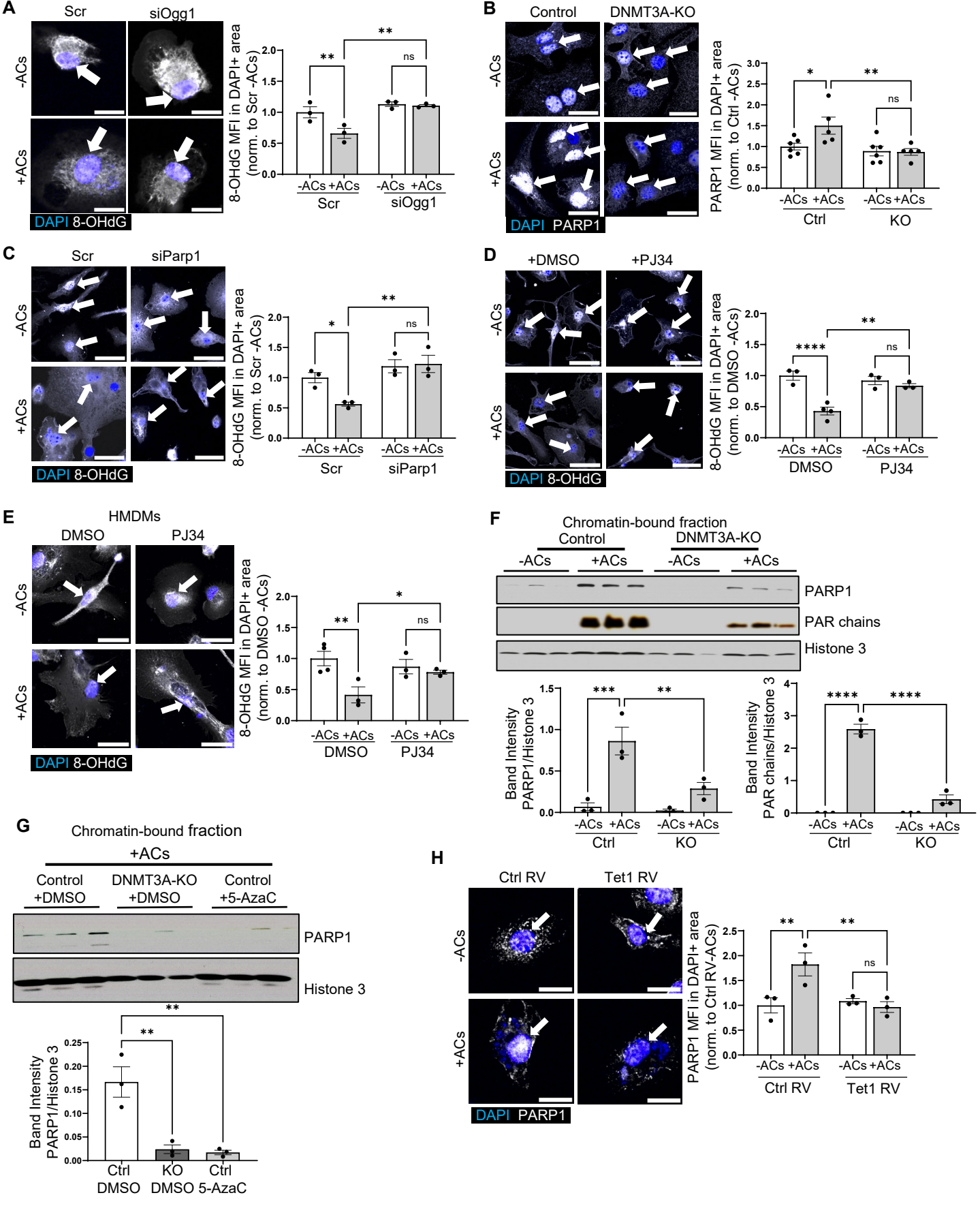
A
Scr
siOgg1
-ACs
+ACs
DAPI 8-OHdG
8-OHdG MFI in DAPI+ area (norm. to Scr -ACs)
-ACs +ACs
Scr
siOgg1
B
Control
DNMT3A-KO
DAPI PARP1
PARP1 MFI in DAPI+ area (norm. to Ctrl -ACs)
Ctrl
KO
C
Scr
siParp1
DAPI 8-OHdG
8-OHdG MFI in DAPI+ area (norm. to Scr -ACs)
siParp1
D
+DMSO
+PJ34
DAPI 8-OHdG
8-OHdG MFI in DAPI+ area (norm. to DMSO -ACs)
DMSO
PJ34
E
HMDMs
DMSO
PJ34
DAPI 8-OHdG
8-OHdG MFI in DAPI+ area (norm. to DMSO -ACs)
F
Chromatin-bound fraction
Control
DNMT3A-KO
PARP1
PAR chains
Histone 3
Band Intensity PARP1/Histone 3
Band Intensity PAR chains/Histone 3
G
Chromatin-bound fraction
+ACs
Control +DMSO
DNMT3A-KO +DMSO
Control +5-AzaC
PARP1
Histone 3
Band Intensity PARP1/Histone 3
Ctrl DMSO
KO DMSO
Ctrl 5-AzaC
H
Ctrl RV
Tet1 RV
DAPI PARP1
PARP1 MFI in DAPI+ area (norm. to Ctrl RV-ACs)

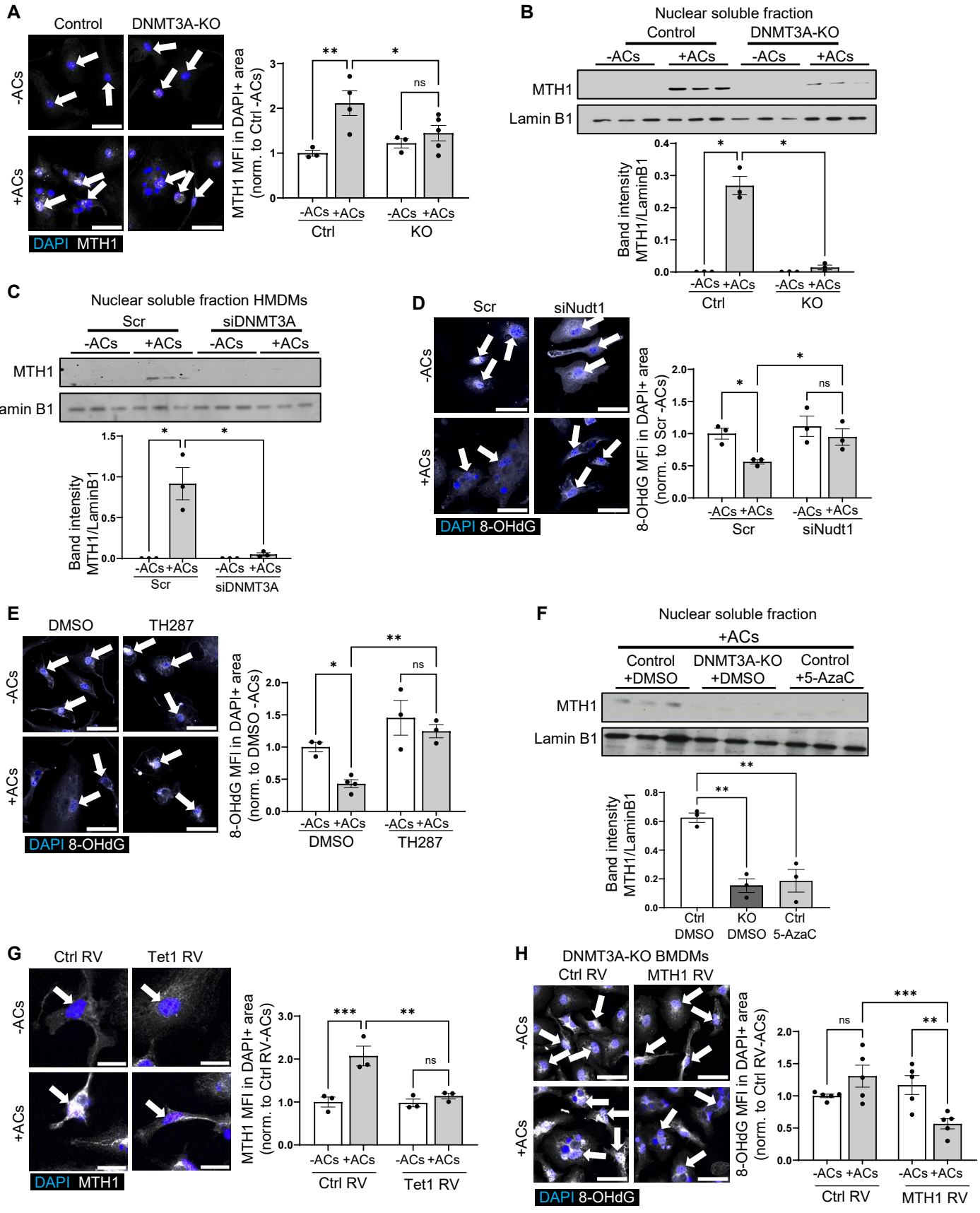
A
Control
DNMT3A-KO
-ACs
+ACs
DAPI MTH1
MTH1 MFI in DAPI+ area (norm. to Ctrl -ACs)
-ACs +ACs
Ctrl
KO
B
Nuclear soluble fraction
Control
DNMT3A-KO
MTH1
Lamin B1
Band intensity MTH1/LaminB1
C
Nuclear soluble fraction HMDMs
Scr
siDNMT3A
Scr
siDNMT3A
D
Scr
siNudt1
DAPI 8-OHdG
8-OHdG MFI in DAPI+ area (norm. to Scr -ACs)
siNudt1
E
DMSO
TH287
8-OHdG MFI in DAPI+ area (norm. to DMSO -ACs)
F
Nuclear soluble fraction
+ACs
Control +DMSO
DNMT3A-KO +DMSO
Control +5-AzaC
Ctrl DMSO
KO DMSO
Ctrl 5-AzaC
G
Ctrl RV
Tet1 RV
MTH1 MFI in DAPI+ area (norm. to Ctrl RV-ACs)
H
DNMT3A-KO BMDMs
Ctrl RV
MTH1 RV
8-OHdG MFI in DAPI+ area (norm. to Ctrl RV-ACs)

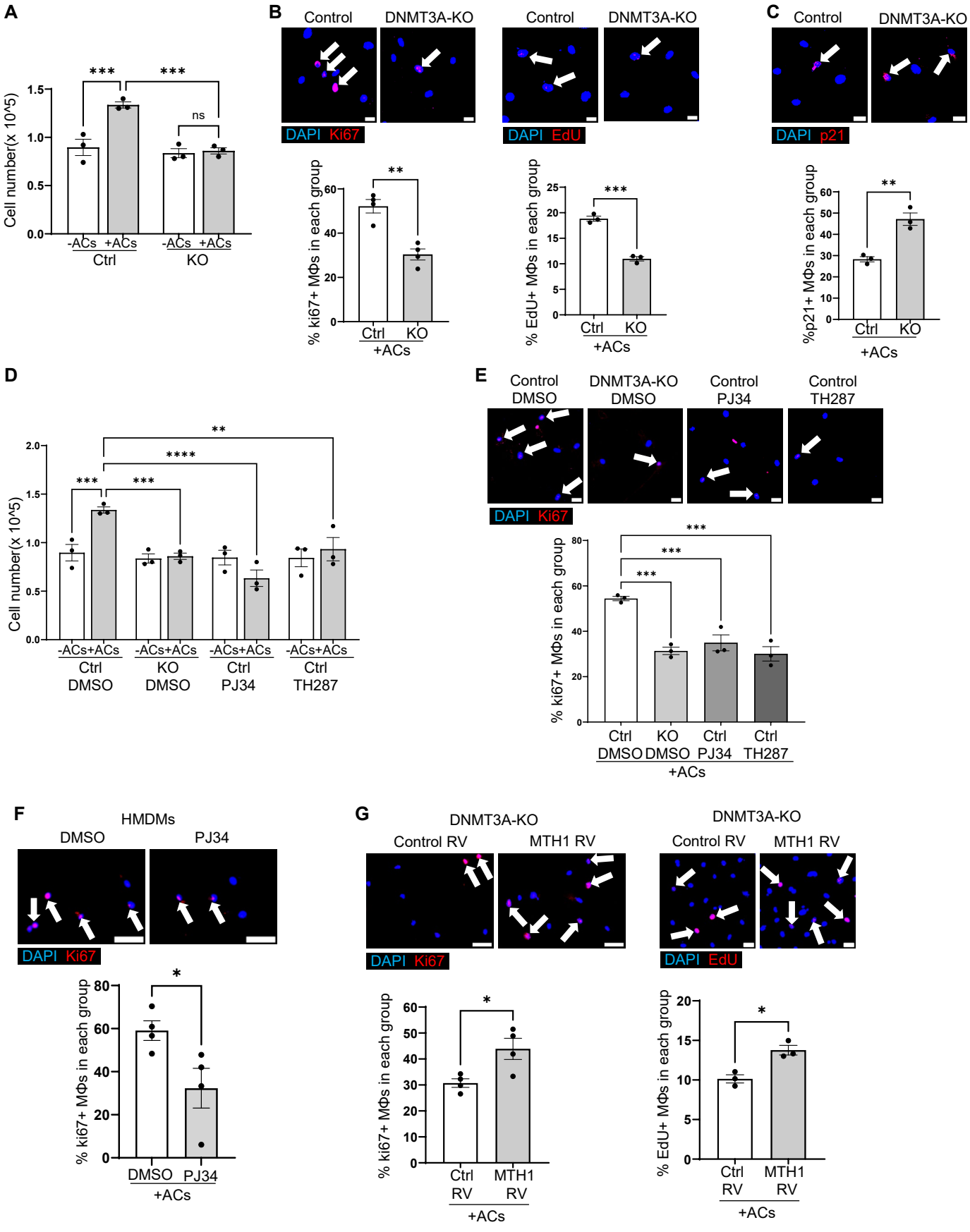
A
Cell number(x 10^5)
***
***
ns
-ACs +ACs
Ctrl
-ACs +ACs
KO
B
Control
DNMT3A-KO
DAPI Ki67
% ki67+ MΦs in each group
**
Ctrl KO
+ACs
Control
DNMT3A-KO
DAPI EdU
% EdU+ MΦs in each group
***
Ctrl KO
+ACs
C
Control
DNMT3A-KO
DAPI p21
%p21+ MΦs in each group
**
Ctrl KO
+ACs
D
Cell number(x 10^5)
**
****
***
***
-ACs+ACs
Ctrl
DMSO
-ACs+ACs
KO
DMSO
-ACs+ACs
Ctrl
PJ34
-ACs+ACs
Ctrl
TH287
E
Control
DMSO
DNMT3A-KO
DMSO
Control
PJ34
Control
TH287
DAPI Ki67
% ki67+ MΦs in each group
***
***
***
Ctrl
DMSO
KO
DMSO
Ctrl
PJ34
Ctrl
TH287
+ACs
F
HMDMs
DMSO
PJ34
DAPI Ki67
% ki67+ MΦs in each group
*
DMSO PJ34
+ACs
G
DNMT3A-KO
Control RV
MTH1 RV
DAPI Ki67
% ki67+ MΦs in each group
*
Ctrl
RV
MTH1
RV
+ACs
DNMT3A-KO
Control RV
MTH1 RV
DAPI EdU
% EdU+ MΦs in each group
*
Ctrl
RV
MTH1
RV
+ACs

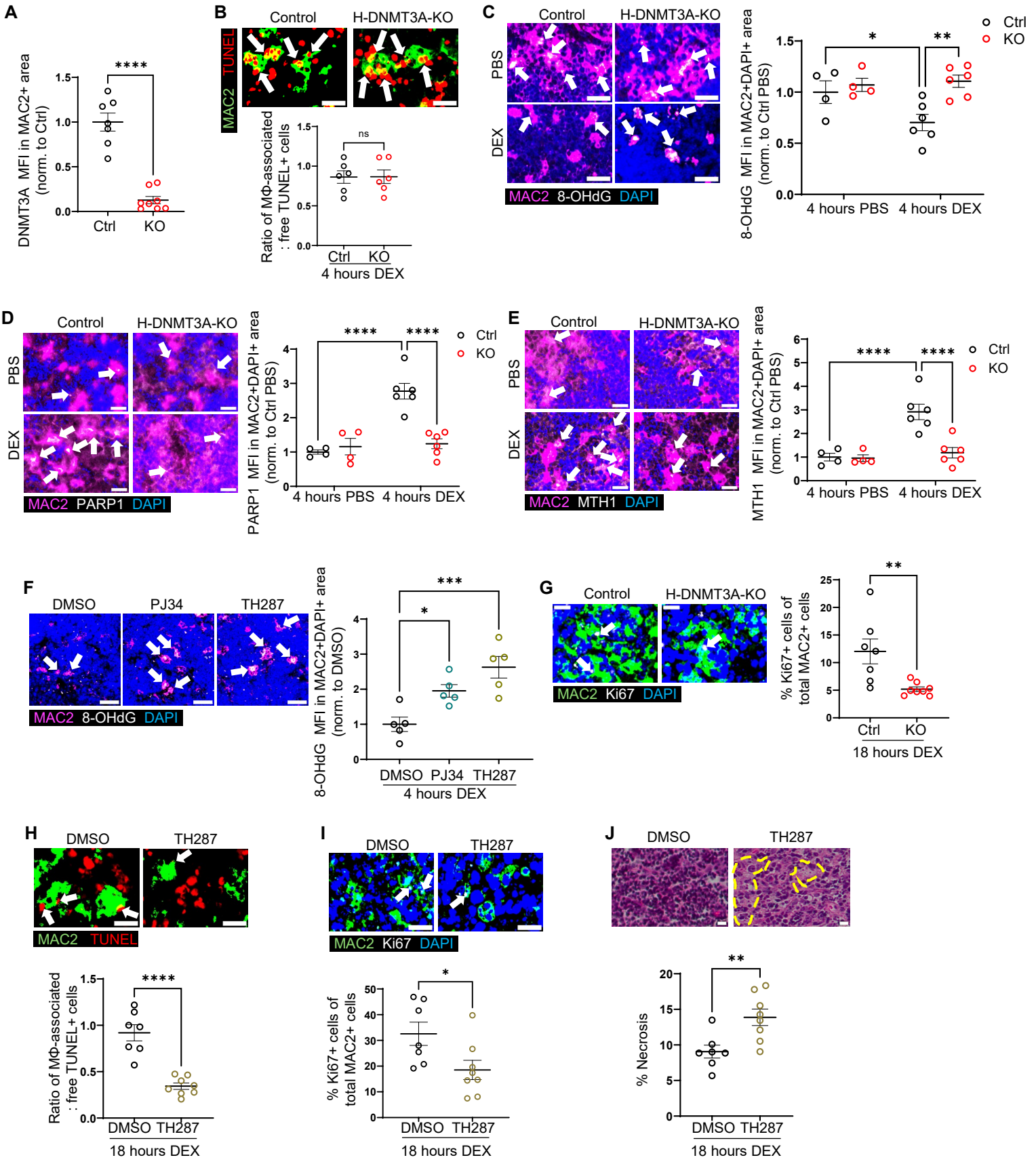
A
DNMT3A MFI in MAC2+ area (norm. to Ctrl)
****
Ctrl
KO
B
Control
H-DNMT3A-KO
MAC2 TUNEL
Ratio of MΦ-associated : free TUNEL+ cells
ns
Ctrl
KO
4 hours DEX
C
Control
H-DNMT3A-KO
PBS
DEX
MAC2 8-OHdG DAPI
8-OHdG MFI in MAC2+DAPI+ area (norm. to Ctrl PBS)
*
**
Ctrl
KO
4 hours PBS
4 hours DEX
D
Control
H-DNMT3A-KO
PBS
DEX
MAC2 PARP1 DAPI
PARP1 MFI in MAC2+DAPI+ area (norm. to Ctrl PBS)
****
****
Ctrl
KO
4 hours PBS
4 hours DEX
E
Control
H-DNMT3A-KO
PBS
DEX
MAC2 MTH1 DAPI
MTH1 MFI in MAC2+DAPI+ area (norm. to Ctrl PBS)
****
****
Ctrl
KO
4 hours PBS
4 hours DEX
F
DMSO
PJ34
TH287
MAC2 8-OHdG DAPI
8-OHdG MFI in MAC2+DAPI+ area (norm. to DMSO)
***
*
DMSO
PJ34
TH287
4 hours DEX
G
Control
H-DNMT3A-KO
MAC2 Ki67 DAPI
% Ki67+ cells of total MAC2+ cells
**
Ctrl
KO
18 hours DEX
H
DMSO
TH287
MAC2 TUNEL
Ratio of MΦ-associated : free TUNEL+ cells
****
DMSO
TH287
18 hours DEX
I
DMSO
TH287
MAC2 Ki67 DAPI
% Ki67+ cells of total MAC2+ cells
*
DMSO
TH287
18 hours DEX
J
DMSO
TH287
% Necrosis
**
DMSO
TH287
18 hours DEX

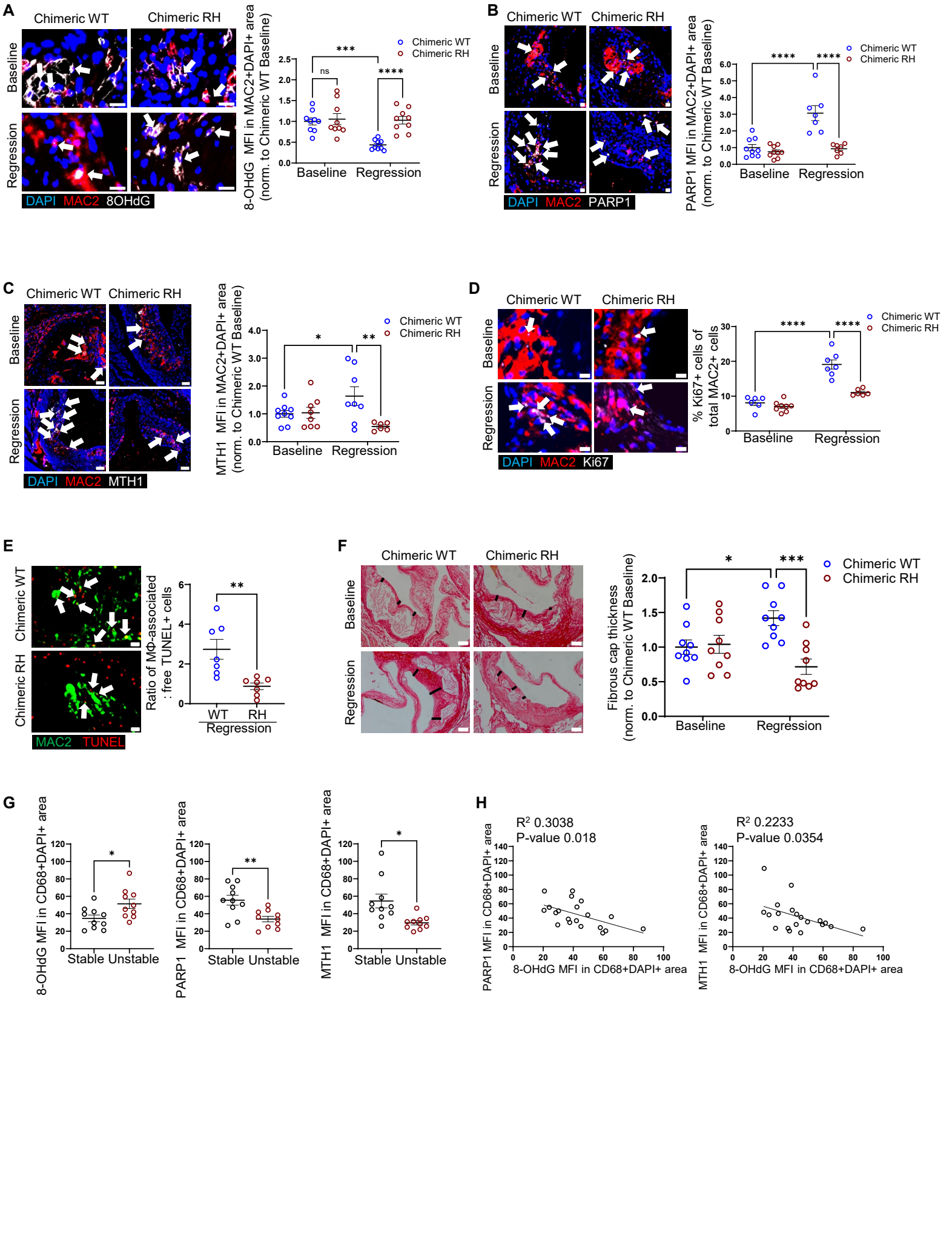
A
Chimeric WT
Chimeric RH
Baseline
Regression
DAPI MAC2 8OHdG
8-OHdG MFI in MAC2+DAPI+ area (norm. to Chimeric WT Baseline)
Chimeric WT
Chimeric RH
***
ns
****
Baseline
Regression
B
Chimeric WT
Chimeric RH
Baseline
Regression
DAPI MAC2 PARP1
PARP1 MFI in MAC2+DAPI+ area (norm. to Chimeric WT Baseline)
Chimeric WT
Chimeric RH
****
****
Baseline
Regression
C
Chimeric WT
Chimeric RH
Baseline
Regression
DAPI MAC2 MTH1
MTH1 MFI in MAC2+DAPI+ area (norm. to Chimeric WT Baseline)
Chimeric WT
Chimeric RH
*
**
Baseline
Regression
D
Chimeric WT
Chimeric RH
Baseline
Regression
DAPI MAC2 Ki67
% Ki67+ cells of total MAC2+ cells
Chimeric WT
Chimeric RH
****
****
Baseline
Regression
E
Chimeric WT
Chimeric RH
MAC2 TUNEL
Ratio of MΦ-associated : free TUNEL+ cells
**
WT
RH
Regression
F
Chimeric WT
Chimeric RH
Baseline
Regression
Fibrous cap thickness (norm. to Chimeric WT Baseline)
Chimeric WT
Chimeric RH
*
***
Baseline
Regression
G
8-OHdG MFI in CD68+DAPI+ area
*
Stable
Unstable
PARP1 MFI in CD68+DAPI+ area
**
Stable
Unstable
MTH1 MFI in CD68+DAPI+ area
*
Stable
Unstable
H
R² 0.3038
P-value 0.018
PARP1 MFI in CD68+DAPI+ area
8-OHdG MFI in CD68+DAPI+ area
R² 0.2233
P-value 0.0354
MTH1 MFI in CD68+DAPI+ area
8-OHdG MFI in CD68+DAPI+ area